Using a Green's Function Approach to Diagnose the Pattern Effect in GFDL AM4 and CM4

BOSONG ZHANG,[a] MING ZHAO,[b] AND ZHIHONG TAN[a]

[a] *Program in Atmospheric and Oceanic Sciences, Princeton University, Princeton, New Jersey*
[b] *NOAA/Geophysical Fluid Dynamics Laboratory, Princeton, New Jersey*

(Manuscript received 20 January 2022, in final form 25 October 2022)

ABSTRACT: Global radiative feedbacks exhibit large dependence on the spatial structure of sea surface temperature (SST) changes, which is referred to as the "pattern effect." A Green's function (GF) approach has been demonstrated to be useful in identifying and understanding contributions of regional SST changes to global radiative feedbacks. Here, we explore the ability of the GF approach in quantifying the pattern effect in an atmospheric model (AM4) and a coupled model (CM4) recently developed at NOAA's Geophysical Fluid Dynamics Laboratory (GFDL), including the impact of SST changes on global-mean and local responses of key variables important to climate. Given historical SST patterns, the GF derived from idealized experiments with SST warming patches can largely reproduce AM4 simulated global-mean and regional responses. When AM4 is forced by SST patterns retrieved from the CM4 abrupt quadrupling of carbon dioxide experiment, the same GF captures interannual variations of AM4 simulated global-mean responses but falls short of reproducing the magnitude of the responses. A decomposition of such SST patterns into global-mean values plus remaining anomalies helps reduce biases. Additional idealized experiments are conducted to examine the sensitivity of the GF to the amplitude and sign of SST perturbations and to the integration time and the confidence level of the significance test. Impacts of these factors on the performance of the GF are discussed.

KEYWORDS: Sea surface temperature; Climate sensitivity; Feedback; Climate models

1. Introduction

Historical records indicate that sea surface temperatures (SSTs) exhibit an overall warming in response to increasing concentration of atmospheric greenhouse gases (Cheng et al. 2019). However, SST changes are not spatially uniform. Uncertainties remain large at regional scales in terms of the magnitude of warming and its spatial structure including zonal and meridional SST gradients. Recent studies using observations and general circulation models (GCMs) showed that warming over the eastern Pacific and Southern Oceans is delayed (Andrews et al. 2015; Armour et al. 2016; Luo et al. 2017). The delayed Southern Ocean warming is argued to be shaped by the Southern Ocean's meridional overturning circulation (Armour et al. 2016). Overall, the observed warming pattern may be modulated by natural variability (Olonscheck et al. 2020; Watanabe et al. 2021), aerosol–cloud interactions (Wang et al. 2021), and changes in sea surface salinity (Liu et al. 2021), among many other factors.

While different processes contribute to the spatial structure of SST changes, in turn, the spatial structure of SST changes can modulate radiative feedbacks (Bony et al. 2006; Soden et al. 2008). The sensitivity of radiative feedbacks to the spatial structure (i.e., patterns) of surface warming is referred to as the pattern effect (Stevens et al. 2016). Armour et al. (2013) considered a local feedback framework in which local radiative responses are only attributed to local temperature changes. In comparison, recent studies suggest that feedbacks exhibit large sensitivity to the spatial structure of SST changes, which includes both local and remote effects (Rose et al. 2014; Andrews et al. 2015; Rose and Rayborn 2016; Zhou et al. 2016; Ceppi and Gregory 2017; Andrews and Webb 2018). Using a single atmosphere-only model, the amplitude of global radiative feedback was demonstrated to vary substantially for simulations forced by different SST patterns with identical global-mean SST warming (Zhao 2022). In addition, the amplitude of radiative feedback can vary between different periods (Andrews et al. 2015, 2022). The time dependence of radiative feedback can be contributed by individual components. For example, Fueglistaler and Silvers (2021) showed that global average shortwave cloud radiative feedback as a function of global average surface temperature is positive before 1970s but changes sign and becomes negative after that. A better understanding of the observed radiative feedback could help constrain long-term feedback (He et al. 2021).

Given the strong dependence of radiative feedbacks on the spatial structure of SST changes, Zhou et al. (2017) proposed a way in which the feedbacks in response to a specific warming pattern can be estimated by a Green's function (GF) approach. They showed that this approach can largely capture the change of cloud feedback in response to changes in atmospheric CO_2 concentration. Dong et al. (2019) used the GF approach to attribute global-mean radiative feedbacks to spatial patterns of SST changes. They showed that the GF approach can largely reproduce interannual variations of the

Supplemental information related to this paper is available at the Journals Online website: https://doi.org/10.1175/JCLI-D-22-0024.s1.

Corresponding author: Bosong Zhang, bosongzhang@gmail.com

DOI: 10.1175/JCLI-D-22-0024.1

global-mean radiative feedbacks in both the historical and the abrupt 4 × CO_2 simulations provided their time evolution of SSTs. They found that the global-mean net top-of-atmosphere (TOA) radiation is more sensitive to SST warming over the tropical western Pacific than SST warming over other regions. However, since the GF approach requires a suite of sensitivity simulations in a specific GCM, results retrieved from the GF can be model dependent. An intermodel comparison project about the GF approach using different GCMs can provide more insights into how well the GF approach reproduces model projections of future climate change. In addition to the GF approach, Bloch-Johnson et al. (2020) argued that the dependence of radiative feedbacks on the spatial structure of SST changes can be estimated using multiple regression in fully coupled models. However, as shown in Ceppi and Fueglistaler (2021), changes in tropical radiative budget are out of phase with El Niño–Southern Oscillation (ENSO), indicating a two-way coupling between SST and radiation.

In this study, we apply the GF approach to a state-of-the-art GCM and assess the extent to which several select variables from the model's historical simulations and future projections can be reproduced by the GF. The GF is derived from a suite of atmosphere-only simulations with patches of anomalous SSTs added to the climatological-mean SSTs. We use the derived GF to reconstruct climate responses from an atmosphere-only simulation forced by historically observed SSTs and SSTs simulated from an atmosphere–ocean coupled simulation with abrupt quadrupling of atmospheric CO_2 concentration. In addition to comparisons of global-mean values between model-simulated ones and the GF reconstructed ones, regional patterns are also examined. In terms of the sensitivity experiments with patches of SST anomalies, we test whether and how the amplitude and sign of SST anomalies affect the performance of the GF approach. The primary goal of this study is to evaluate and understand how the GF may or may not reproduce model-simulated signals under different conditions.

2. Methods

a. The Green's function

Following Zhou et al. (2017), we use the discrete form of the GF approach, which computes the change of a variable X (e.g., net TOA radiation, surface air temperature, and so on) at a grid point i in response to perturbations in SST as

$$\Delta X_i = \sum_{j=1}^{n} \frac{\partial X_i}{\partial \mathrm{SST}_j} \Delta \mathrm{SST}_j + \varepsilon_X, \tag{1}$$

where $\Delta \mathrm{SST}_j$ represents the change of SST at a grid point j. The first-order term on the right-hand side of this equation represents a linear combination of the responses at all ocean grid points. Other second-order and higher-order terms are denoted by the residual term ε_X. This framework assumes one can emulate the model-simulated climate response of a variable X given the term $\partial X_i/\partial \mathrm{SST}_j$ and $\Delta \mathrm{SST}_j$ without running any numerical simulations. Given that the GF defined in Eq. (1) does not consider the impact of changes in radiative forcing, sea ice, and other components in the climate system, the GF reconstruction is not supposed to exactly capture responses from coupled simulations. Instead, the GF here is supposed to only capture the response due to SST anomalies by construction. Note that the surface temperature over land (also known as the skin temperature over land) in this approach is regarded as the "response" instead of the "forcing," and it is assumed to vary only with SST perturbations. It is possible that the impact of surface temperature changes over land is considered in a different version of the GF approach. However, such modification complicates comparisons between the results in this study and the prior results based on Eq. (1). Thus, we leave potential attempts to include the impact of surface temperature changes over land to future studies.

In Eq. (1), $\partial X_i/\partial \mathrm{SST}_j$ can be written as a Jacobian matrix that is referred to as $\mathscr{J}_X(i,j)$. In this framework, $\Delta \mathrm{SST}_j$ is needed to quantify ΔX_i if the Jacobian matrix is available and does not change with time. However, to compute the Jacobian matrix, a suite of idealized experiments forced by patches of SST anomalies are required in advance. Although the Jacobian matrix is time independent, $\Delta \mathrm{SST}_j$ can be either time-dependent or long-term climatological values. One common practice of visualizing the GF is to show maps of global annual-mean responses of state variables per unit SST warming in each grid box, that is, $[\overline{\mathscr{J}_X(j)}]$, where the overbar stands for long-term annual mean computed from monthly mean values, and the square bracket stands for a spatial average over the entire globe. With the first dimension of $\mathscr{J}_X(i,j)$ averaged out horizontally, $[\overline{\mathscr{J}_X(j)}]$ illustrates how the change of SST at a grid point j ($\Delta \mathrm{SST}_j$) contributes to global annual-mean responses of a variable X.

b. Experiment design

In this study, we use the Geophysical Fluid Dynamics Laboratory (GFDL) atmospheric model (AM4) model (Zhao et al. 2018a,b) to conduct perturbation experiments forced by patches of anomalous SST. AM4 has a horizontal grid spacing of ~100 km. The default AM4 outputs have 180 grid points in the meridional direction and 288 in the zonal direction (i.e., 1.0° latitude × 1.25° longitude for the horizontal resolution). We note that previous studies mainly apply the GF approach to model outputs of ~2° resolution (Zhou et al. 2017; Dong et al. 2019). In this study, we reinterpolate the default model outputs to a lower horizontal resolution with 90 grid points in the meridional direction and 144 in the zonal direction (i.e., 2.0° latitude × 2.5° longitude for the horizontal resolution).

Per the definition in Eq. (1), the first dimension i and the second dimension j represent grid boxes of varying horizontal area due to changes in a grid's latitude and ocean area fraction. In addition, for model outputs of different horizontal resolutions, an intermodel comparison of the derived Jacobian matrices is more difficult. For example, $\mathscr{J}_X(i,j)$ tends to be larger in magnitude in a lower-resolution model due to its larger area of SST perturbation. To compare $\mathscr{J}_X(i,j)$ derived from outputs of different horizontal resolutions in a standard

TABLE 1. Parameters related to geographic locations of the patches used in the SST perturbation experiments: lat_p is the center latitude and lon_p is the center longitude of the patches. The value lat_p is paired up with lon_p in the same column. Positive (negative) values of lat_p means northern (southern) hemisphere. Values of lon_p mean degrees east; for example, 200° means 160°W. The map of the patches can be found in Fig. S1.

Patches shown in Fig. S1	
lat_p: 0°, ±15°, ±30°, ±50°, ±75°	lat_p: ±7.5°, ±22.5°, ±37.5°, ±62.5°
lon_p: 0°, 40°, 80°, 120°, 160°, 200°, 240°, 280°, 320°	lon_p: 20°, 60°, 100°, 140°, 180°, 220°, 260°, 300°, 340°

way, we propose that the actual physical area of a grid box should be considered. In this sense, we consider

$$\frac{[\overline{\mathscr{J}_X(j)}]}{\text{PA}_j}, \tag{2}$$

where PA_j represents actual physical area of a grid box j. Equation (2) stands for global annual-mean responses of state variables per unit SST warming per unit physical area. For example, $[\overline{\mathscr{J}_T(j)}]/\text{PA}_j$ is global annual-mean responses of surface air temperature per unit SST warming per unit physical area (units of K^{-1} km^{-2}). In the rest of the paper, we focus on the normalized Jacobian matrices and use $[\overline{\mathscr{J}_X(j)}]$ for simplicity.

In addition, we note that the size of Jacobian matrices derived from high-resolution outputs are much larger than those derived from low-resolution outputs, which significantly increases computational time and memory use for analyses. However, we find that the Jacobian matrices derived from low-resolution outputs have the same ability as those derived from high-resolution outputs in reproducing global-mean values from an atmosphere-only simulation prescribed with observed SSTs and sea ice concentration. Therefore, we use model outputs of relatively low resolution. In the rest of the paper, we focus on the Jacobian matrices derived from the outputs of ~2° horizontal resolution.

To derive the Jacobian matrix $\mathscr{J}_X(i,j)$, we first conduct a control simulation with AM4 forced by the observed climatological (1981–2014) monthly means of SSTs and sea ice concentrations from PCMDI used in phase 6 of the Coupled Model Intercomparison Project (CMIP6; Eyring et al. 2016). Note that the greenhouse gases and aerosol emissions are from the 2010 condition and are set as constant over the control simulation. The control simulation is integrated for 31 years with the last 30-yr output used to compute the model's mean state. In each perturbation experiment, a patch of constant SST perturbation is added to the climatological monthly means of SSTs used in the control run. Perturbations of SST over each patch are computed following the equation originally proposed by Barsugli and Sardeshmukh (2002) as

$$\Delta\text{SST}(\text{lat},\text{lon}) = A\cos^2\left(\frac{\pi}{2}\frac{\text{lat}-\text{lat}_p}{\text{lat}_w}\right)\cos^2\left(\frac{\pi}{2}\frac{\text{lon}-\text{lon}_p}{\text{lon}_w}\right). \tag{3}$$

The same method is also used in Zhou et al. (2017) and Dong et al. (2019). In Eq. (3), A is a parameter that controls the maximum amplitude of SST anomaly. Positive values of A stand for SST warming, while negative ones stand for cooling. Subscript p denotes the center point of the patch, and subscript w represents the half-width of the patch. While lon_w is set as 40° for all patches, lat_w increases with the absolute values of latitude (see details in Table 1). Figure S1 in the online supplemental material shows locations of the patches used in this study. Details of these parameters in Eq. (3) are provided in Table 1. We note that the center points of patches used in this study are slightly different from those in Dong et al. (2019) due to different model setups. Given a specific value of the parameter A, we conducted 153 SST perturbation experiments with each integrated for 11 years. The results over the last 10 years are used for analyses. As in Dong et al. (2019), insignificant anomalies between the control run and the SST perturbation runs are set as zero. The significance of anomalies is assessed by the two-sided Student's t test at the 95% confidence level. Insignificant anomalies are regarded as "noise" due to limited model integration time. To explore the sensitivity of the GF to the parameter A, we conducted three suites of SST perturbation experiments with $A = +1.5$, $+4.0$, and -4.0 K. The integration time is the same for 11 years with the last 10 years used for analyses. Moreover, we run another suite of SST perturbation experiments with $A = +1.5$ K and each experiment integrated for 31 years. These additional experiments aim at investigating the sensitivity of the GF to the integration time and the confidence level. Table 2 lists these experiments.

To evaluate the performance of the GF approach, we compare the GF reconstruction with an atmosphere-only simulation forced by observed SSTs and sea ice concentrations from 1870 to 2014 using AM4. The atmosphere-only simulation is forced by preindustrial radiative gases and aerosol emissions throughout the 1870–2014 period and is referred to as the Amip-piForcing simulation. The Amip-piForcing simulation is equivalent to the historical simulation used in Dong et al. (2019). Also, we utilize a coupled simulation in coupled model (CM4; Held et al. 2019) with an abrupt 4 times increase of atmospheric CO_2 concentration. The CM4 simulation was integrated for 150 years and is referred to as the CM4 4 × CO_2 simulation, which was branched off from CM4 preindustrial control simulation (referred to as CM4 pi-Control) that had been integrated for several hundreds of years. Both CM4 pi-Control and CM4 4 × CO_2 simulations are identical to the GFDL's submission to CMIP6. An overview of the effective climate sensitivity in CM4 can be found in Winton et al. (2020) and Zhao (2022). Following Dong et al. (2019), we conduct an AM4 simulation with a time evolution of monthly SST and sea ice anomalies from CM4 4 × CO_2 relative to

TABLE 2. A list of the simulations conducted in this study. The asterisk means that group iv is the same as group i except that the integration time for group iv is longer.

Experiment name	SST forcing	Integration time	Definition of climatology
Control	Monthly varying climatology of SST averaged over 1981–2014	31 years	Monthly climatology averaged over the last 30 years of the simulation
Patch simulations	(i) $A = +1.5$ K (ii) $A = +4.0$ K (iii) $A = -4.0$ K (iv) $A = +1.5$ K*	11 years for groups i–iii; 31 years for group iv	Monthly climatology averaged over the last 10 years of the simulation for groups i–iii, over the last 30 years of the simulation for group iv
Amip-piForcing simulation	Monthly varying observed historical SSTs	145 years from 1870 to 2014	Monthly climatology averaged from 1870 to 1899
CM4 4 × CO_2	Coupled simulation with abrupt quadrupling of CO_2; SST is model generated	150 years	—
AM4 4 × CO_2	Atmosphere-only simulation with monthly varying climatology of SST used in the control run plus monthly varying SST anomalies from CM4 4 × CO_2 relative to its piControl experiment	150 years	—
Plus2K	Atmosphere-only simulation with monthly varying climatology of SST used in the control run plus uniform 2-K warming	31 years	Monthly climatology averaged over the last 30-yr simulations

CM4 pi-Control added to the monthly varying climatology used in the control run (referred to as AM4 4 × CO_2). Compared to the CM4 4 × CO_2 simulation, there is no coupling and no changes in the concentration of CO_2 in the AM4 4 × CO_2 simulation. Therefore, it is a clean way of applying the GF to the AM4 4 × CO_2 simulation in the absence of actual changes in CO_2. In addition, a Plus2K experiment with uniform 2-K warming added to the SST condition in the control run is conducted (Table 2).

3. Results

a. Global annual-mean responses

Figure 1 shows maps of global annual-mean responses per unit SST warming per square kilometer retrieved from the SST perturbation experiments with $A = +4.0$ K. The Indo-Pacific warm pool is characterized by negative values of net TOA radiation (Fig. 1a), positive values of surface air temperature (Fig. 1b), and negative radiative feedback (Fig. 1c). These results are qualitatively consistent with those found in CAM4 and CAM5 (Zhou et al. 2017; Dong et al. 2019). The tropical Atlantic and the tropical northeastern Pacific also stand out as regions important for producing strong negative radiative feedback in AM4 (Fig. 1c), which is generally missing in CAM4 (Dong et al. 2019) but is discernable in CAM5 (Zhou et al. 2017), indicating significant model dependence of the GF. An ongoing Green's Function Model Intercomparison Project (GFMIP; J. Bloch-Johnson et al. 2023, unpublished manuscript) will focus more on the intermodel spread. Overall, the global-mean response of net cloud radiative effect (CRE; Fig. 1f) is consistent with that of low-cloud amount (Fig. 1i), the global-mean response of the longwave (LW) component of CRE (Fig. 1e) is consistent with that of high-cloud amount (Fig. 1h), and the global-mean response of the shortwave (SW) component of CRE (Fig. 1d) is consistent with that of total cloud amount (Fig. 1g). However, the CRE responses to local SST warming can be dominated by either the LW or SW component. For example, SST warming over the tropical Atlantic and the northeastern Pacific induces negative global-mean CRE responses (Fig. 1f), which is dominated by the negative responses of the LW component of CRE (Fig. 1e) that owes to a decrease in global-mean high-cloud amount (Fig. 1h).

With SST perturbations, the GF approach can be used to reconstruct climate responses. Figure 2 compares the GF reconstructed global annual-mean responses with actual model-simulated ones. The response for the Amip-piForcing run is defined by removing monthly climatology averaged from 1870 to 1899, while that for the AM4 4 × CO_2 run is defined by removing monthly climatology from the 30-yr simulation of the control run. For the Amip-piForcing run, the GF approach generally reproduces interannual variations of net TOA radiation, surface air temperature, and radiative feedback (Figs. 2a–c), which is consistent with the results in CAM4 (Dong et al. 2019). In terms of the AM4 4 × CO_2 run, the GF approach underestimates the magnitude of negative net TOA radiation and positive surface air temperature responses (Figs. 2d,e), although the GF reconstructed radiative feedback appears to match the model-simulated ones well (Fig. 2f). Note that the impact of changes in sea ice is not considered here. Given that a reduction in sea ice increases the global-mean net TOA radiative fluxes and surface

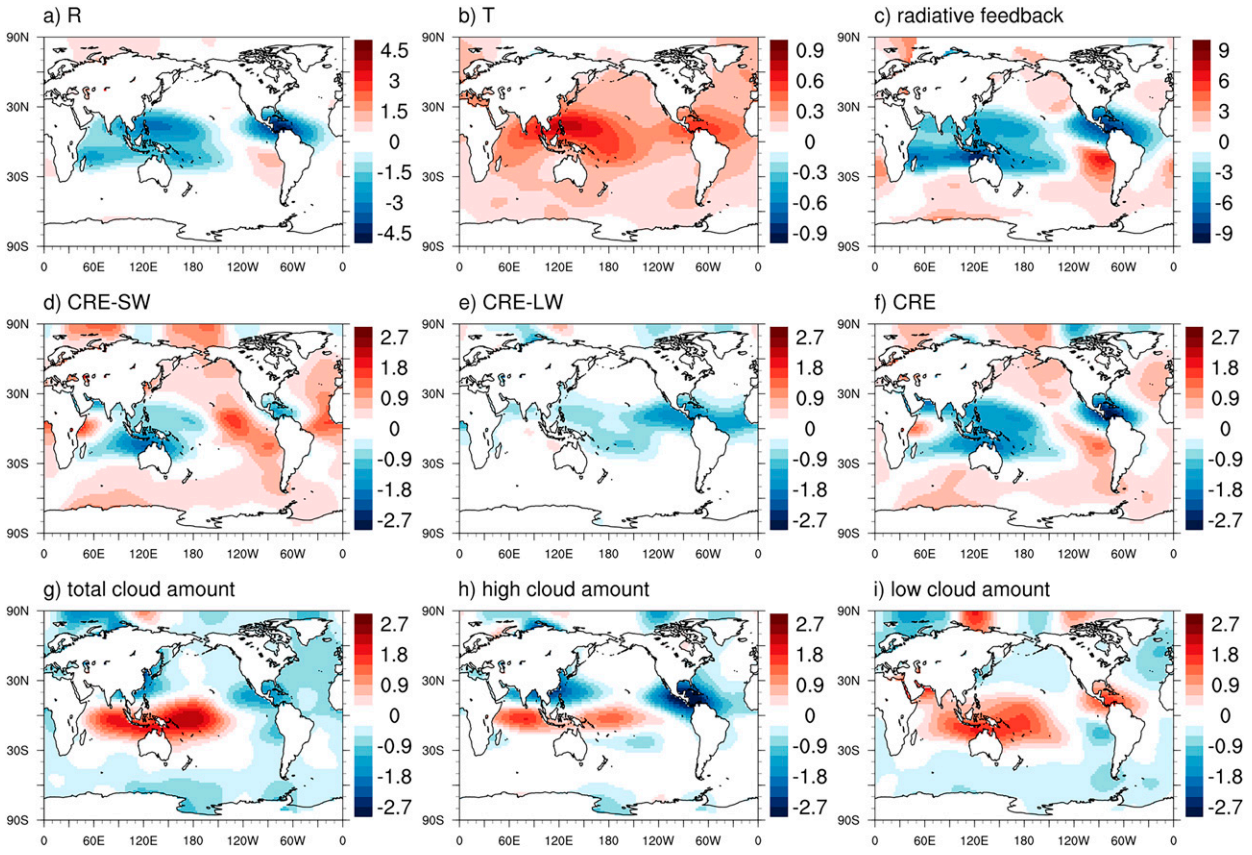

FIG. 1. Maps of global annual-mean (a) net TOA radiation, (b) surface air temperature, (c) radiative feedback, (d) shortwave component of cloud radiative effect (CRE-SW), (e) longwave component of cloud radiative effect (CRE-LW), (f) total CRE, (g) total cloud amount, (h) high-cloud amount, and (i) low-cloud amount in response to 1-K local SST warming at each ocean grid point (values are normalized by actual physical area of each grid box). Note that values between -1.5×10^{-9} and -1.5×10^{-9} in (b) are masked to avoid potential infinity issues in (c). The unit for (a), (d), (e), and (f) is $\times 10^{-8}$ W m^{-2} K^{-1} of local SST warming per km^2, for (b) the unit is $\times 10^{-8}$ K^{-1} of local SST warming per km^2, for (c) the unit is W m^{-2} K^{-1} of global-mean surface air temperature warming (actual physical area has been canceled out), and for (g)–(i) the unit is $\times 10^{-8}$% K^{-1} of local SST warming per km^2. For example, for a value of -1.6×10^{-8} over the western Pacific in (a), it indicates a change of global annual-mean net radiation at TOA of -1.6×10^{-8} W m^{-2} in response to 1-K SST warming over 1-km^2 region.

air temperature (Zhao 2022), taking into account the impact of sea ice can to some extent reduce the biases between the GF reconstruction and the model simulations, as shown in Dong et al. (2019). Further discussion on the impact of sea ice can be found at the end of this section.

We further decompose the net TOA radiation into clear-sky, CRE, net LW, and net SW components. For the AmipPiForcing run, the GF approach largely captures interannual variations of the clear-sky (Fig. 3a) and net LW (Fig. 3c) components. However, the reconstructed CRE (Fig. 3b) and net SW (Fig. 3d) components exhibit some biases in recent decades. For the AM4 4 × CO_2 run, it turns out that the biases in Fig. 2d are mostly from the CRE rather than the clear-sky component (Figs. 3e,f). In comparison, the GF approach yields stronger LW cooling and SW heating (Figs. 3g,h).

Several factors may contribute to the differences between the GF reconstructed values and the model-simulated ones. Primarily, the GF reconstructed CRE exhibits more biases than the clear-sky component (Fig. 3), which is probably due to the nonlinear behavior of convection to SST perturbations. For the total net TOA radiation and surface air temperature, Dong et al. (2019) proposed a way in which the impact of changes in sea ice has been added to the reconstructed responses. However, biases still exist [see Fig. 7 in Dong et al. (2019)]. They argued that nonlinearity in global-mean net TOA radiation associated with either global-mean or local temperature change cannot explain why the GF reconstructed values are biased from model-simulated ones. The GF derived from experiments with SST patches of limited domain sizes cannot capture relatively uniform warming or cooling SST patterns, which potentially puts a limitation for the use of the GF approach. This has been mentioned in Dong et al. (2019). One possibility is that the relationship between convection and SST is intrinsically nonlinear. The climate response tends to be linear when a small number of individual SST patches are perturbed at the same time. However, an underlying prerequisite is that these limited number of patches should be located far away enough from each other, which applies to the two-patch

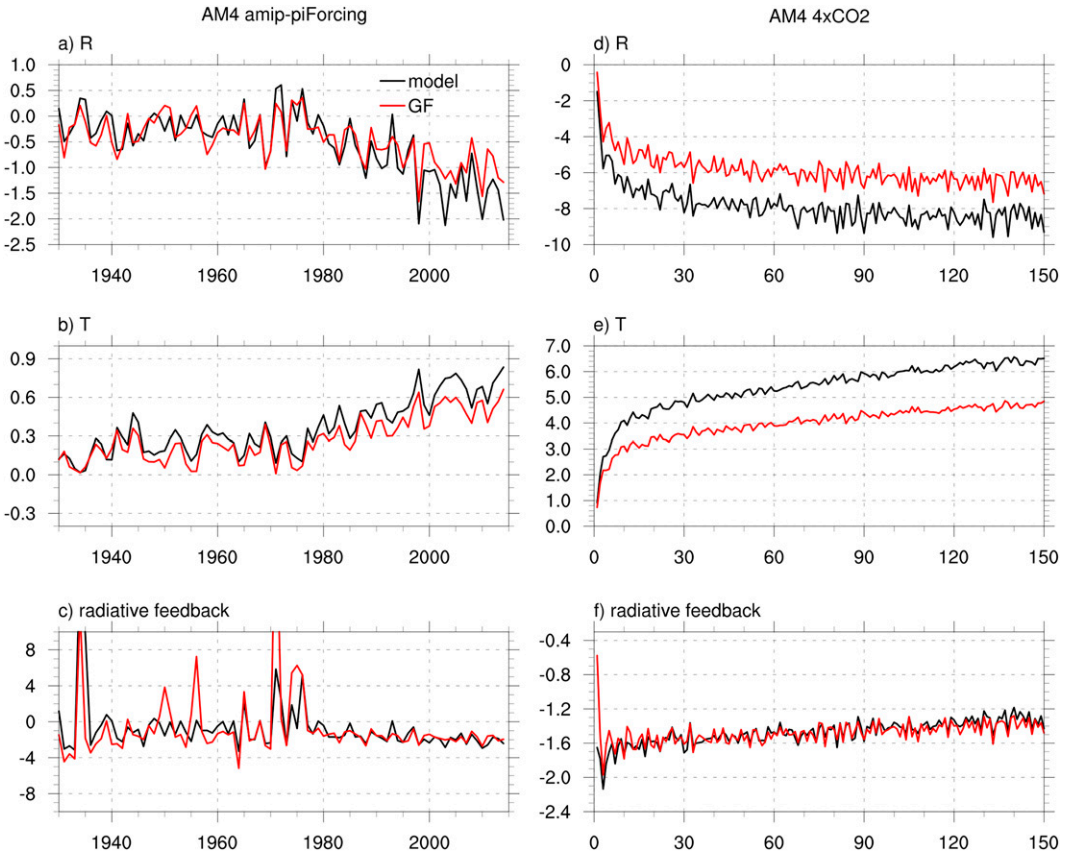

FIG. 2. (a),(d) The global annual-mean response for net TOA radiation (W m^{-2}), (b),(e) surface air temperature (K), and (c),(f) radiative feedback (W m^{-2} K^{-1}) retrieved from the (left) AM4 Amip-piForcing run and (right) AM4 4 × CO_2 run. The black solid lines show actual model simulations, while the red solid lines show the GF reconstruction. The response for the Amip-piForcing run is defined by removing monthly climatology averaged from 1870 to 1899, while that for the AM4 4 × CO_2 run is defined by removing monthly climatology from the control run. For each experiment, radiative feedback is computed with net TOA radiation over surface air temperature.

run shown in Dong et al. (2019). However, this may break up when more patches are considered at the same time and/or the parches stay closer to each other, where a uniform warming scenario can be regarded as an extreme case for this.

While the GF reconstructed values are biased from the model-simulated ones for AM4 4 × CO_2 run, we note that the overall trend in Figs. 2 and 3 is largely captured by the GF. Also, compared with the SST patterns in the Amip-piForcing run, the SST patterns in the AM4 4 × CO_2 run are more spatially uniform in terms of the warming trend. Therefore, we decompose the total SST patterns in the AM4 4 × CO_2 run into two parts:

$$\Delta \mathrm{SST}_{4\times \mathrm{CO}_2} = \Delta[\mathrm{SST}_{4\times \mathrm{CO}_2}] + \Delta \mathrm{SST}^*, \tag{4}$$

where $\Delta \mathrm{SST}_{4\times \mathrm{CO}_2}$ represents the original SST warming patterns used in Figs. 2 and 3 for the AM4 4 × CO_2 run; $\Delta[\mathrm{SST}_{4\times \mathrm{CO}_2}]$ is the global-mean component and is a function of time only; and $\Delta \mathrm{SST}^*$ is the departure from the global-mean value, which represents "the remaining SST patterns." With such decomposition, we can apply the GF approach to $\Delta \mathrm{SST}^*$ to account for the impact of "the remaining SST patterns" and scale responses from uniform SST warming experiment (e.g., the Plus2K run) with actual global-mean SST warming in the AM4 4 × CO_2 run ($[\Delta[\mathrm{SST}_{4\times \mathrm{CO}_2}]$) to account for the impact of global-mean trend. For the AM4 4 × CO_2 run, the final reconstructed values for a certain variable X involve two parts:

$$\Delta[X_{4\times \mathrm{CO}_2}] = \frac{\Delta[X]_{\mathrm{p2K}}}{2K} \times \Delta[\mathrm{SST}_{4\times \mathrm{CO}_2}] + \mathscr{J}_X \times \Delta \mathrm{SST}^*. \tag{5}$$

For the first term on the right-hand side of Eq. (5), the model-simulated response from the Plus2K run ($\Delta[X]_{\mathrm{p2K}}$) is scaled by the global-mean SST warming in the AM4 4 × CO_2 run. The second term on the right-hand side is using the Jacobian matrix $\mathscr{J}_X$ to reconstruct the impact of "the remaining SST patterns." Through this, biases in net TOA radiation and surface air temperature are reduced compared to the original reconstruction (Figs. 4a,b). For individual components of net TOA radiation, the modified GF based on Eq. (5) shows improvement (Figs. 4d–g). These results indicate that the default GF approach is unable to reproduce the magnitude of the responses for individual components of net TOA radiation

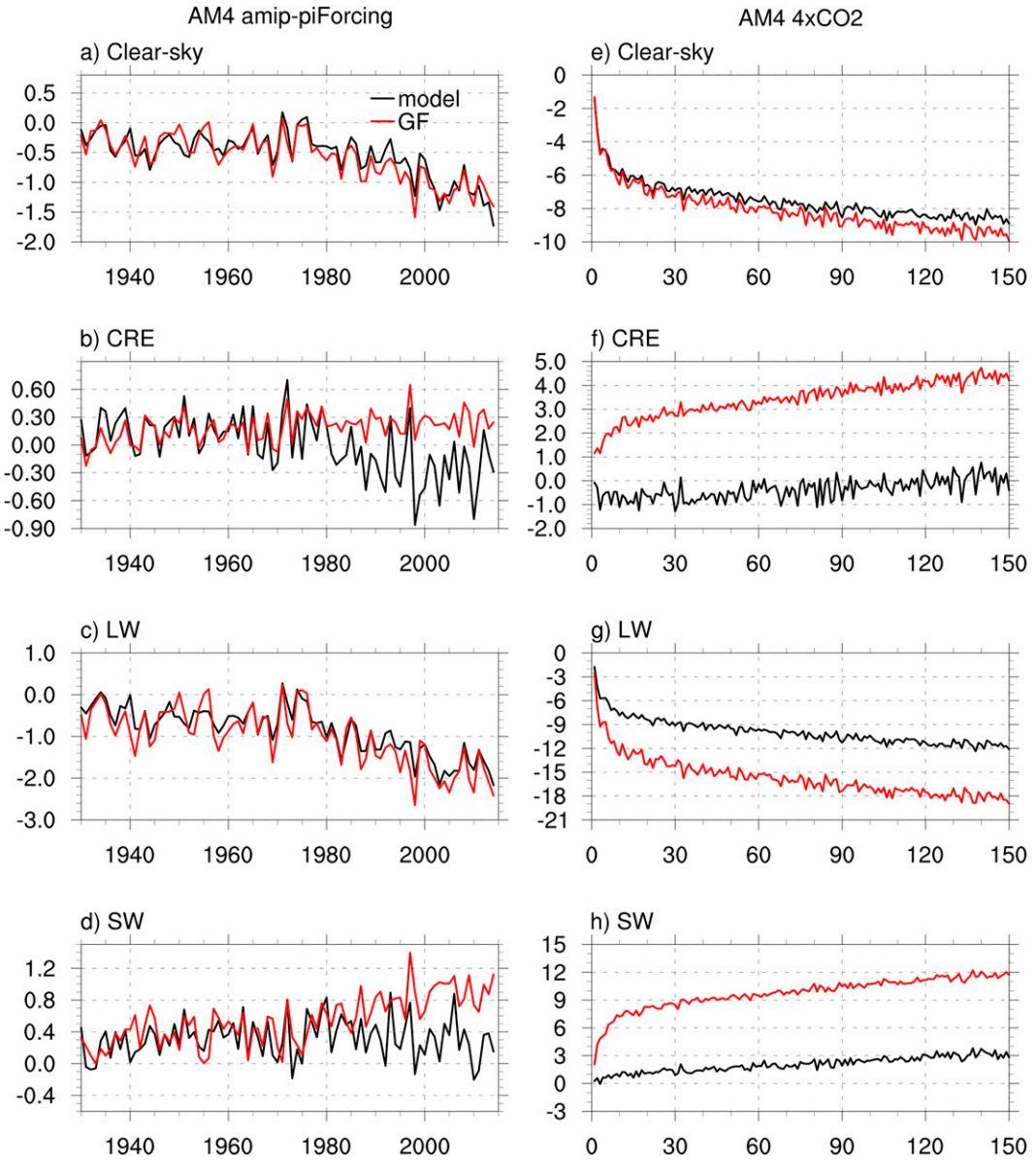

FIG. 3. The global annual-mean response for (a),(e) clear-sky net TOA radiation, (b),(f) cloud radiative effect, (c),(g) net LW radiation at TOA, and (d),(h) net SW radiation at TOA retrieved from the (left) AM4 Amip-piForcing run and (right) AM4 4 × CO_2 run. The black solid lines show actual model simulations while the red solid lines show the GF reconstruction.

when there is an overall warming trend. The modified GF based on Eq. (5) does a better job, although it still has some issues like reproducing the magnitude of CRE (Fig. 4e). Nevertheless, the significant improvement by Eq. (5) indicates that the large biases shown in Fig. 3 are mostly caused by the uniform warming part. Given the complex behavior of convection to SST perturbation, it is not surprising that the GF has issues in reproducing the response associated with the uniform warming part. Thus, separately accounting for the impact from the uniform warming part should be considered a useful complement to the original GF approach.

In terms of the original GF approach, there could be multiple reasons why the GF reconstructed global-mean values are biased from model-simulated ones: (i) surface temperature changes over land are regarded as response instead of forcing in the GF approach, which is also mentioned in section 2a. The derived Jacobian matrices are multiplied with surface temperature changes over ocean. Given that the response of surface temperature over land to SST perturbations involves a lot of processes, the linear assumption of the GF may not be good enough to capture the response over land in general. (ii) There is a coupling between changes in surface temperature

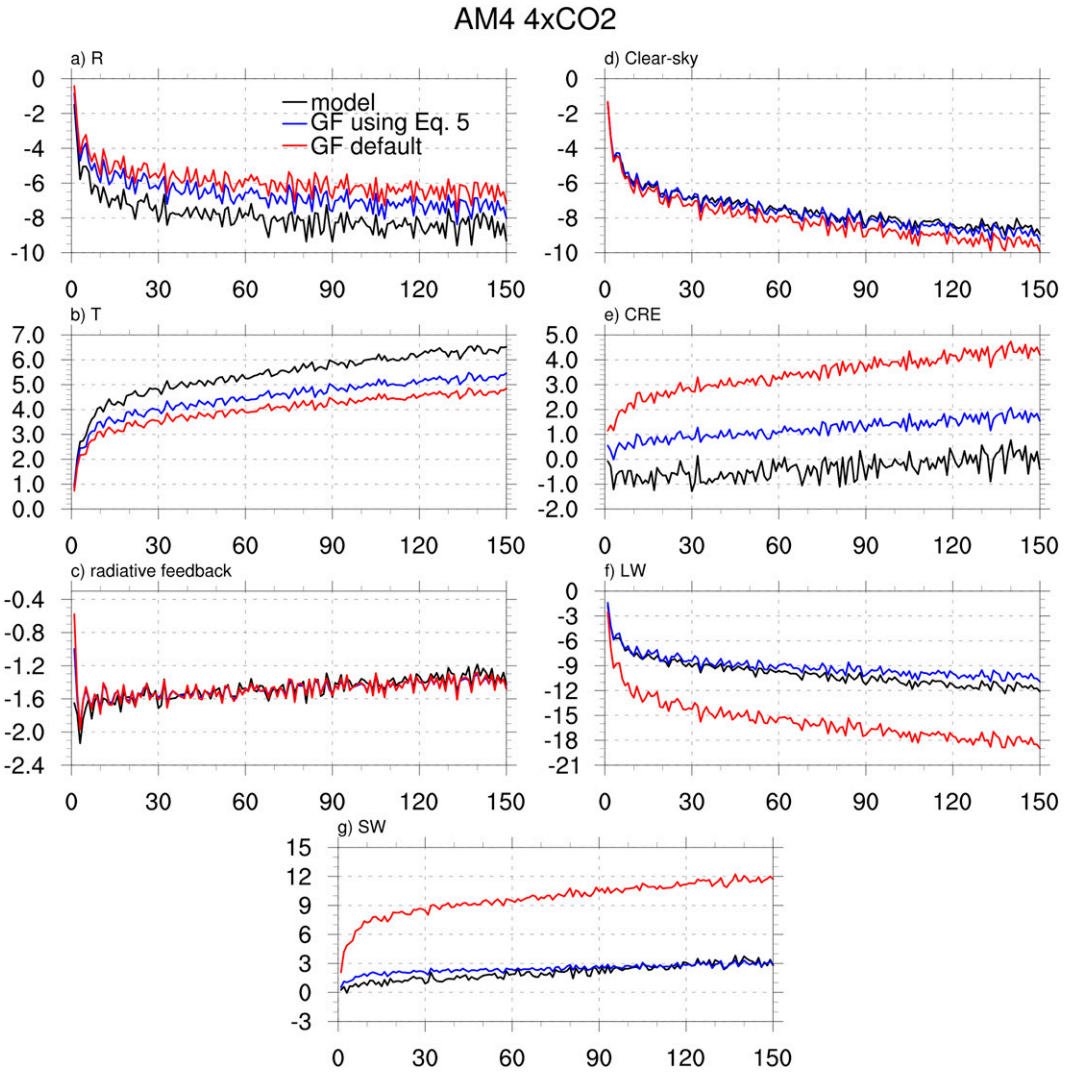

FIG. 4. The global-annual-mean response for (a) net TOA radiation, (b) surface air temperature, (c) radiative feedback, (d) clear-sky net TOA radiation, (e) cloud radiative effect, (f) net LW radiation at TOA, and (g) net SW radiation at TOA for the AM4 4 × CO_2 run. The black solid lines show actual model simulations. The red solid lines show the default GF reconstruction as in Figs. 2 and 3. The blue solid lines show a combination of the GF reconstruction and scaled responses retrieved from AM4 experiment with uniform +2-K SST warming based on Eq. (5).

over land and changes in other variables such as cloud, which is not considered by the GF. (iii) The impact of sea ice is not addressed in this paper. Although Dong et al. (2019) proposed a way in which the impact of sea ice is considered, a tunable parameter is used to control the proportion of the impact of sea ice. Essentially, the tunable parameter itself brings in extra uncertainty. In addition, it remains unclear whether changes in sea ice and changes in SST should be considered simultaneously by assuming that the changes in sea ice are proportional to the changes in SST, as has been done in Dong et al. (2019), or if the changes of the two variables should be considered individually. In the latter case, idealized experiments in which only sea ice is perturbed but SST remains the same would be conducted to derive the Jacobian matrices purely due to changes in sea ice. There is no simple answer in terms of which one is more appropriate. To test the difference is beyond the scope of this paper. Future studies can explore this.

b. *Regional responses*

Future climate change requires information of regional responses for key variables (e.g., surface air temperature, precipitation, etc.) that are useful for local policy making. In this section, we explore the extent to which the GF reproduces regional responses given different SST patterns. We consider three modes of natural oscillation with significant changes in SST patterns: (i) ENSO, (ii) the Atlantic multidecadal oscillation (AMO), and (iii) the Indian Ocean dipole (IOD). Variations of ENSO are measured by the Niño-3.4 index (Trenberth 1997), which is the SST anomaly averaged over

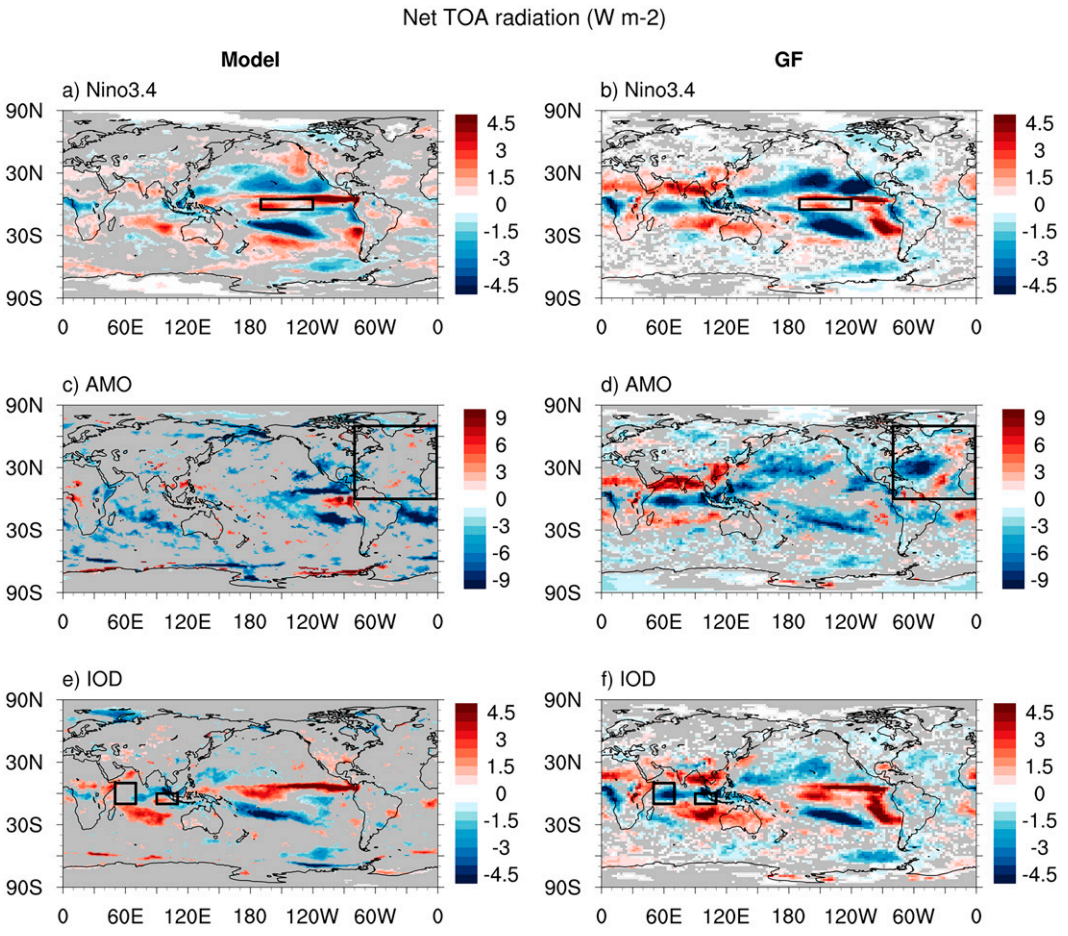

FIG. 5. Maps of net TOA radiation (W m^{-2}) retrieved from the Amip-piForcing run regressed against (a) the Niño-3.4 index, (c) the AMO index, and (e) the IOD index. The GF reconstruction is shown for (b) the Niño-3.4 index, (d) the AMO index, and (f) the IOD index. Grid points that are insignificant at 95% level are in gray color. The black rectangles in each subplot show the geographic location for each index. See section 3b for more details.

the region 5°S–5°N and 190°–240°E. A 3-month running average is applied to the domain-averaged SST. For the AMO, we use the detrended SST averaged over the North Atlantic (0°–70°N) and a 121-month running average is applied to get the AMO index (Enfield et al. 2001). The IOD is measured by the difference in SST anomalies between the western equatorial Indian Ocean (50°–70°E and 10°S–10°N) and the southeastern equatorial Indian Ocean (90°–110°E and 10°S–0°), which is usually referred to as the dipole mode index (DMI; Saji et al. 1999). For actual model outputs from the Amip-piForcing run, variables are regressed against these indices at each grid point. For the GF, we first regress historically observed SST against these indices to get SST patterns. Next, we use the Jacobian matrices and the regressed SST patterns to reconstruct regional responses.

From central to eastern Pacific, positive Niño-3.4 index (i.e., the El Niño condition) is associated with a narrow band of anomalous radiative heating in the deep tropics but anomalous radiative cooling in the subtropics (Fig. 5a). The GF reconstruction generally reproduces the spatial structure of radiative perturbations over the Pacific, although biases are found over regions like the Indian Ocean (Fig. 5b). For radiative perturbations associated with the AMO index, the model-simulated signals are generally noisy and negligible over the North Atlantic (Fig. 5c), while the GF reconstruction shows large changes (Fig. 5d). The IOD exhibits a similar pattern of radiative perturbations compared to the Niño-3.4 index (Fig. 5e). However, the reconstructed responses are overestimated over Southeast Asia (Fig. 5f).

Compared to net TOA radiation, the spatial structure of surface air temperature from the actual model outputs is better reconstructed by the GF for all three cases, although the GF reconstructed responses over land tend to be more biased compared to those over ocean (Fig. 6). Since surface air temperature is more closely connected with SST compared to net TOA radiation, it comes as no surprise that its spatial structure is better reconstructed by the GF. The same is true for other variables that are tightly connected with SST such as upward longwave radiation at the surface (not shown). However, we note that one major issue about the reconstruction of

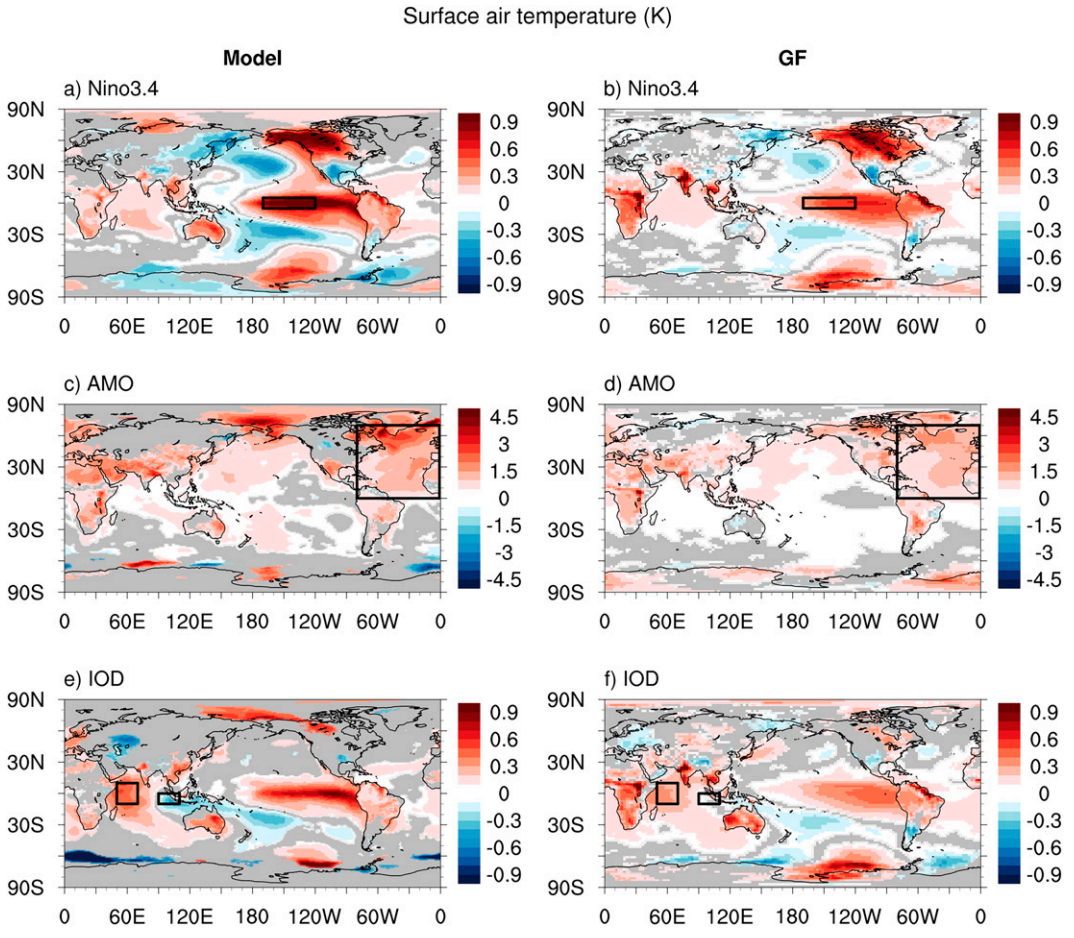

FIG. 6. As in Fig. 5, but for surface air temperature (K).

surface air temperature lies in the amplitude. For example, the GF reconstruction underestimates the warming over the eastern Pacific in the ENSO case (Fig. 6b). Similar issues are found in the IOD case where cooling over the eastern Indian Ocean and warming over the eastern Pacific tend to be weaker in the reconstruction (Fig. 6f). One potential reason is that the size of patches used in the perturbation experiments are in general larger than the typical narrow band of SST anomalies associated with ENSO. Thus, the derived GF may not fully resolve regional details. In any case, this indicates that not only spatial structure but also the amplitude of the GF reconstructed regional responses can vary from case to case, which could be ignored if only global-mean responses are analyzed. Therefore, there is still plenty of room for improvement of the GF in reproducing regional responses.

Additionally, we explore the extent to which the GF reproduces regional responses in precipitation. Both the model-simulated responses and the reconstruction show that precipitation is reduced over the western Pacific but enhanced from central to eastern Pacific for regression against the Niño-3.4 index. However, the GF exhibits large biases over central America (Figs. 7a,b). For the AMO, positive anomalies over central America and the tropical Atlantic (Fig. 7c) are reproduced by the GF (Fig. 7d). However, away from the Atlantic, the reconstruction of precipitation exhibits more biases. In terms of the IOD, the dipole pattern in which positive anomalies over the western Indian Ocean and negative ones over the eastern Indian Ocean (Fig. 7e) is captured by the GF (Fig. 7f).

While the GF can reproduce regional responses from the Amip-piForcing run, we note that the GF cannot fully reproduce regional responses from the AM4 4 × CO_2 run. In section 3a, we show that interannual variations of the global-mean surface air temperature are reproduced by the GF, whereas the global-mean net TOA radiation is overestimated in magnitude by the GF. In fact, the reconstructed regional responses of net TOA radiation and surface air temperature are both biased from the model-simulated ones (not shown). Currently, it remains unclear what causes these regional biases. As mentioned in Dong et al. (2019), the GF approach has limited ability in quantifying feedback when warming signals tend to be spatially uniform (e.g., uniform 2-K SST warming; SST warming induced by quadrupling/doubling of CO_2). Similarly, we find that the GF derived in this study is unable to exactly reproduce the magnitude of the responses from the Plus2K experiment (not shown). One possible reason is related to the linear assumption of the GF approach. The response in a

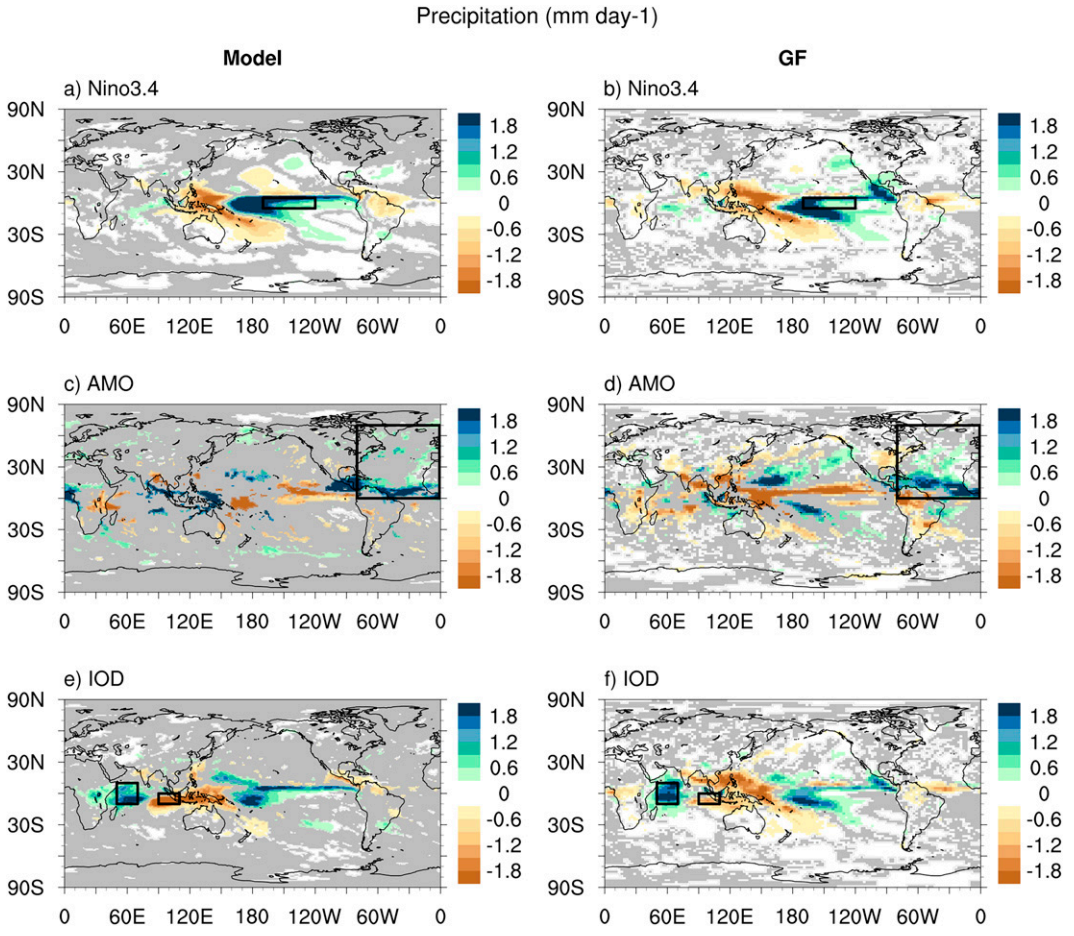

FIG. 7. As in Fig. 5, but for precipitation (mm day^{-1}).

simulation imposed with two individual SST patches simultaneously can be very similar to a linear summation of the responses from these two SST patch experiments [see the linearity test in section 4 of Dong et al. (2019)]. However, this could become invalid when there are more than two individual SST patches imposed at the same time (e.g., greater than 10) and/or when the patches stay closer to each other. The latter scenario is to some extent similar to uniform 2-K SST warming and warming induced by an increase in CO_2. Another possible reason is that atmospheric variability does exist in each of the patch simulations. In terms of the simulations used to derive the GF, each simulation only has a single SST patch. Given relatively spatially uniform SST warming patterns, the linearity may break up, and the derived GF could fail in reproducing responses from simulations such as the AM4 4 × CO_2 run. Future studies need to address the reconstruction of both global and regional responses.

c. *Sensitivity of the GF to the amplitude and sign of SST perturbation*

In sections 3a and 3b, we focus on the Jacobian matrices derived from idealized experiments with $A = +4.0$ K. However, it remains unclear whether and how the amplitude and sign of SST perturbation would impact the performance of the GF in reproducing global and regional responses. Dong et al. (2019) set the parameter A as +1.5 K for nonpolar patches and +3.0 K for polar patches in their SST perturbation experiments. Zhou et al. (2017) examined the linearity of the patch experiments with the parameter A set as ±4.0 and ±2.0 K. They found a mostly linear relationship between the global-mean cloud feedback and the amplitude of SST perturbations. To explore the extent to which the parameter A affects the performance of the GF approach, we conduct two additional suites of experiments in which the parameter A is set as +1.5 and −4.0 K. All the other settings are the same for these experiments (more details can be found in section 2b). We use the parameter A to distinguish the Jacobian matrices. For example, $[\overline{\mathscr{T}_X(j)}]$ derived from the experiments with the parameter $A = +4.0$ K is referred to as the +4.0 K $[\overline{\mathscr{T}_X(j)}]$. In addition, we have another set of Jacobian matrices derived from a combination of the +4.0- and −4.0-K experiments to offset potential nonlinearities associated with the sign of SST perturbation.

We first compare maps of global annual-mean net TOA radiation, surface air temperature, and radiative feedback (Fig. 8). All four Jacobian matrices of net TOA radiation show a negative global-mean TOA radiation response to SST warming over

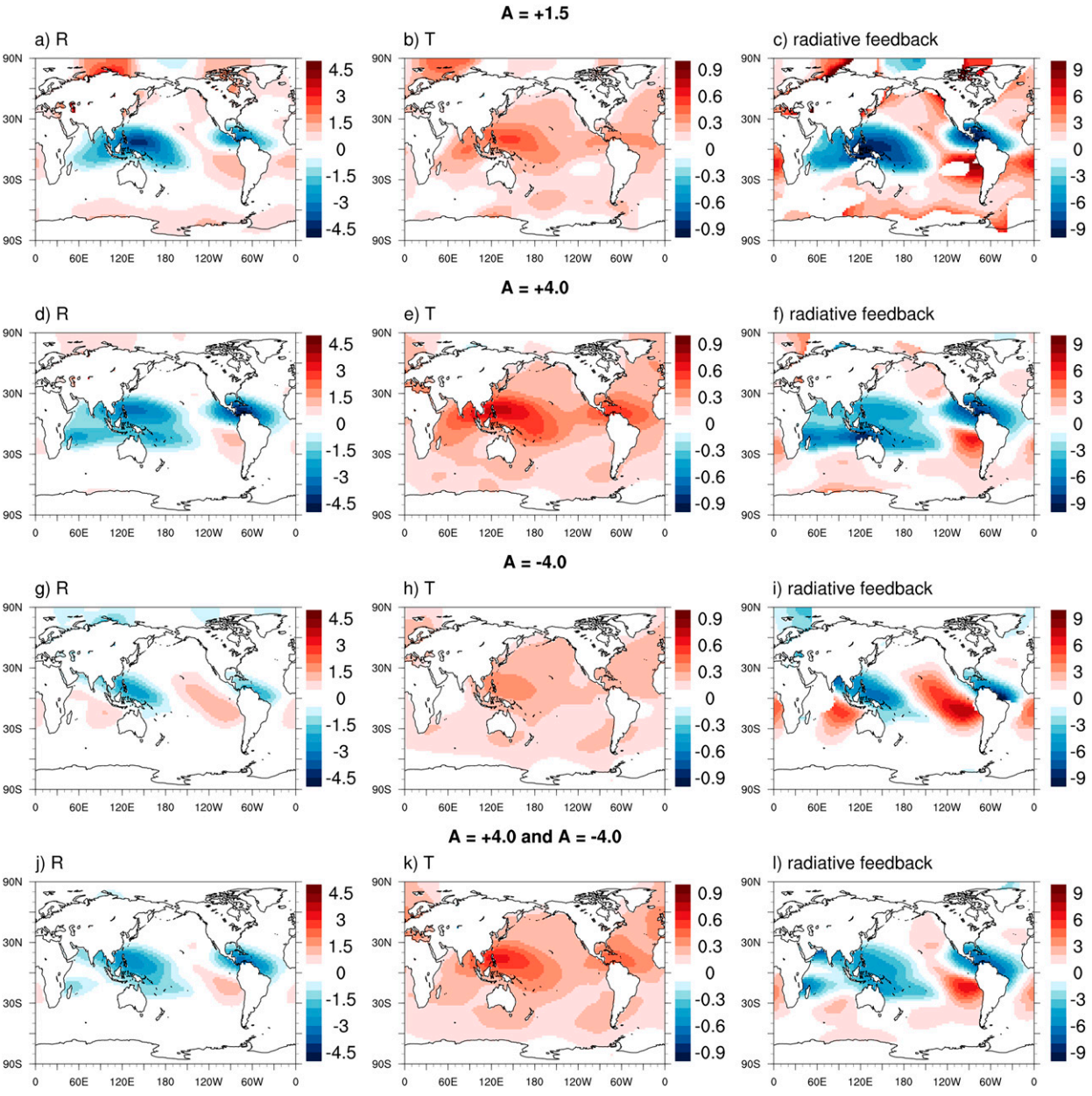

FIG. 8. Maps of global annual-mean responses per unit SST warming normalized by actual physical area of each grid box: (a)–(c) derived from $A = +1.5$ K, (d)–(f) from $A = +4.0$ K, (g)–(i) from $A = -4.0$ K, and (j)–(l) from a combination of $A = +4.0$ and -4.0 K experiments. Note that (a), (d), (g), and (j) are net TOA radiation with units of $\times 10^{-8}$ W m^{-2} per unit local SST warming per km^2; (b), (e), (h), and (k) are surface air temperature with units of $\times 10^{-8}$ K per unit local SST warming per km^2; (c), (f), (i), and (l) are radiative feedback with units of W m^{-2} per 1 K global-mean surface air temperature warming.

the western Pacific. However, for the -4.0 K $[\overline{\mathscr{T}_R(j)}]$ (Fig. 8g), the strength of global-mean radiative cooling over the western Pacific is weaker and its spatial coverage is confined within a smaller region compared to the $+1.5$ K $[\overline{\mathscr{T}_R(j)}]$ (Fig. 8a) and $+4.0$ K $[\overline{\mathscr{T}_R(j)}]$ (Fig. 8d) in which radiative cooling dominates most of the Indo-Pacific warm pool. This indicates that the global-mean net TOA radiation does not respond linearly to SST perturbations in AM4. The absolute amount of anomalous global-mean radiative cooling induced by an increase in SST over the western Pacific is greater than the absolute amount of anomalous global-mean radiative heating induced by a decrease in SST over the same region. To alleviate impacts of the sign of SST perturbation, we derive another set of Jacobian matrices using both the $+4.0$- and -4.0-K experiments. Compared to the $+1.5$ K $[\overline{\mathscr{T}_R(j)}]$ (Fig. 8a) and $+4.0$ K $[\overline{\mathscr{T}_R(j)}]$ (Fig. 8d), the $[\overline{\mathscr{T}_R(j)}]$ derived the $+4.0$- and -4.0-K experiments (Fig. 8j) tends to be smaller in the absolute magnitude of the responses. However, such changes are not linear. In terms of surface air

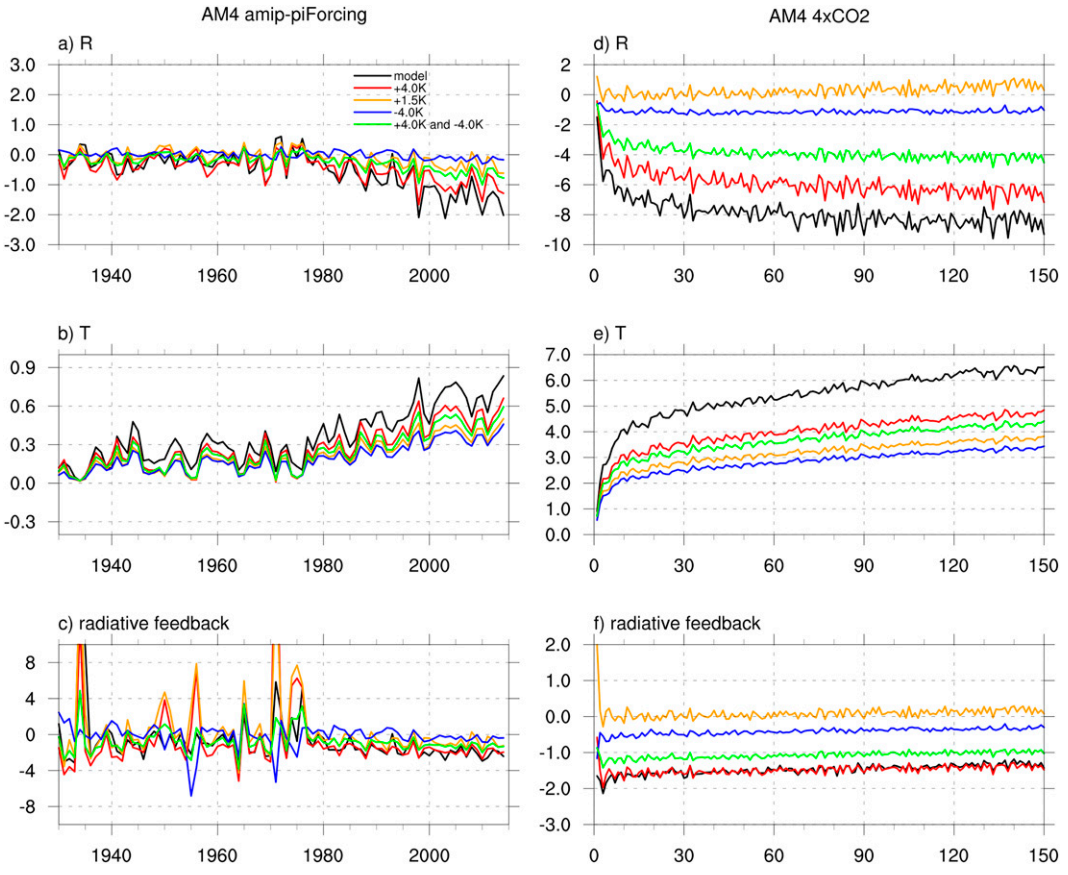

FIG. 9. As in Fig. 2, but comparing the GF reconstruction from $A = +1.5$ K (orange lines), $A = +4.0$ K (red lines), $A = -4.0$ K (blue lines), and a combination of $A = +4.0$ and -4.0 K experiments (green lines).

temperature, the -4.0 K $[\overline{\mathscr{T}_T(j)}]$ (Fig. 8h) exhibits weaker response over the western Pacific compared to the $+1.5$ K $[\overline{\mathscr{T}_T(j)}]$ (Fig. 8b) and the $+4.0$ K $[\overline{\mathscr{T}_T(j)}]$ (Fig. 8e). The weaker response over the western Pacific in the -4.0 K $[\overline{\mathscr{T}_T(j)}]$ is enhanced when the $[\overline{\mathscr{T}_T(j)}]$ is derived from the $+4.0$- and -4.0-K experiments (Fig. 8k). The large differences in $[\overline{\mathscr{T}_R(j)}]$ and $[\overline{\mathscr{T}_T(j)}]$ lead to varied global-mean radiative feedback over the western Pacific (Figs. 8c,f,i,l). One of the hypotheses is about interactions between deep convection and SST. It has been known that tropical deep convection only occurs when moist static energy hits a threshold value (Zhang and Fueglistaler 2019, 2020). Thus, it is possible that convection-induced perturbations (e.g., radiation, clouds, water vapor) exhibit nonlinearity to SST. In addition, the base state in this study (i.e., the control run) is based on the simulation forced by SST climatology averaged from 1981 to 2014. It is possible that the Jacobian matrices exhibit some sensitivity to the base state. The state dependence of the Jacobian matrices requires lots of additional computational resources, which is beyond the scope of this study but can be investigated in future work.

Back to the derived Jacobian matrices in this study, we use them to reconstruct global-mean responses for the Amip-piForcing run and AM4 4 × CO_2 run. In the Amip-piForcing run, the $+1.5$-, $+4.0$-, and combined $+4.0$- and -4.0-K Jacobian matrices show similar ability in reproducing interannual variations of net TOA radiation, surface air temperature, and thus radiative feedback. However, the -4.0-K Jacobian matrices show limited ability in reproducing model-simulated responses (Figs. 9a–c). When it comes to AM4 4 × CO_2 run, the combined $+4.0$- and -4.0-K Jacobian matrices underestimate the magnitude of net TOA radiation and surface air temperature (Figs. 9d–f). The -4.0-K Jacobian matrices can hardly reproduce the model-simulated net TOA radiation, surface air temperature, and radiative feedback (Figs. 9d–f). The $+1.5$-K Jacobian matrices do an even worse job in reproducing the net TOA radiation compared to the -4.0-K ones (Fig. 9d). When decomposing the net TOA radiation into different components (Fig. 10), similar results are found as in Fig. 3. Overall, the GF reconstructed values are biased from model-simulated ones for AM4 4 × CO_2 run. While the amplitude and sign of SST perturbations cannot explain the biases, other factors should be examined in the future.

In addition, we examine the sensitivity of reconstructed regional responses to SST perturbations. Here, we focus on the Niño-3.4 index, which has a well-defined SST pattern associated with robust regional responses. For net TOA radiation and precipitation, the $+1.5$- and $+4.0$-K Jacobian matrices can reproduce their spatial patterns compared to the Amip-piForcing

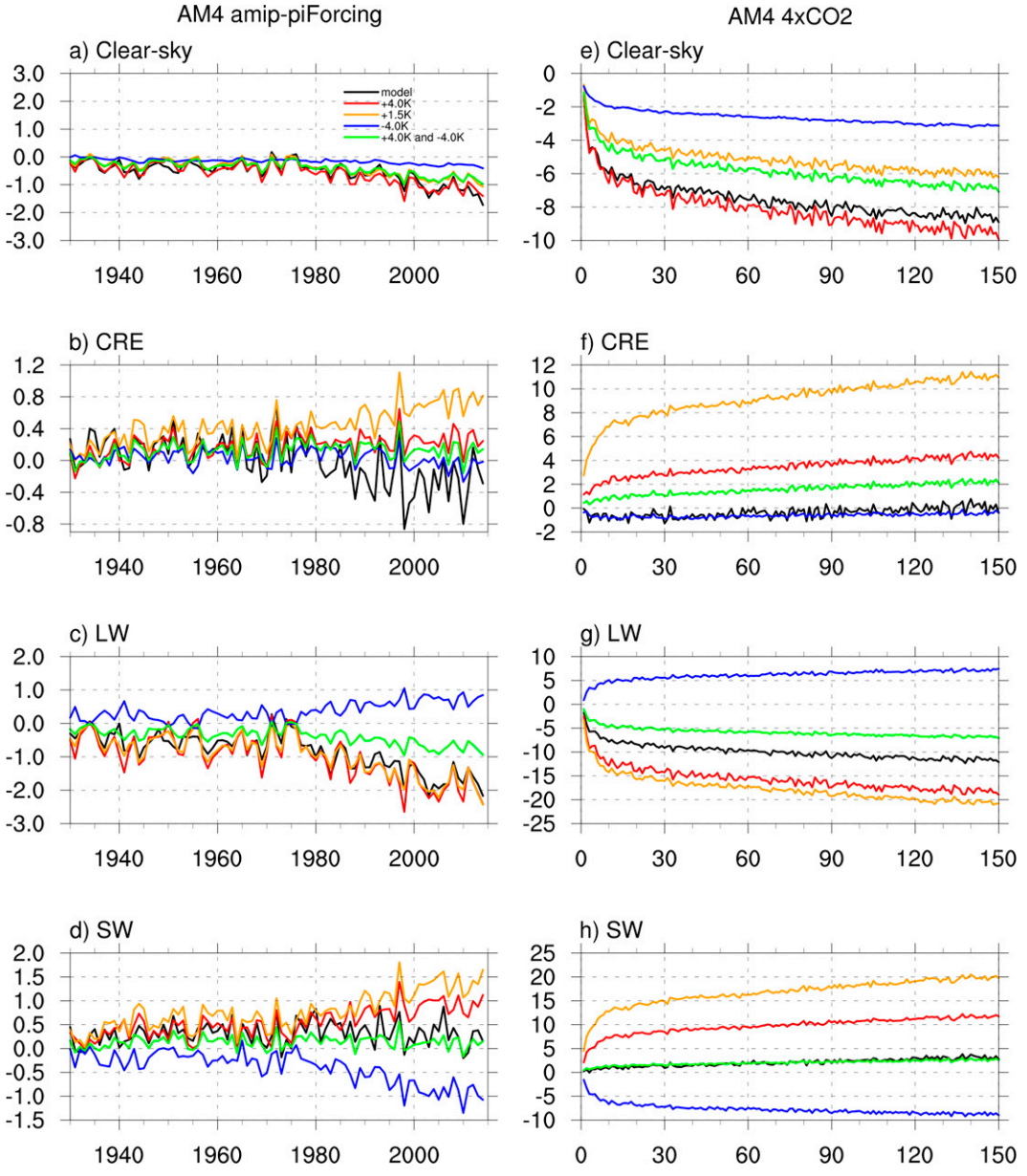

FIG. 10. As in Fig. 3, but comparing the GF reconstruction from $A = +1.5$ K (orange lines), $A = +4.0$ K (red lines), $A = -4.0$ K (blue lines), and a combination of $A = +4.0$ and -4.0 K experiments (green lines).

run. However, we note that the reconstructed net TOA radiation and precipitation from the +4.0-K Jacobian matrices are stronger and more spatially coherent than those from the +1.5-K Jacobian matrices (Fig. 11). The reconstructed regional responses of surface air temperature show smaller difference between these experiments (Fig. 11), which indicates that the amplitude of SST perturbations has limited impact on the reconstruction of regional responses for variables that are tightly connected with SST. On the other hand, the −4.0-K Jacobian matrices cannot reproduce the structure of net TOA radiation and precipitation associated with the Niño-3.4 index. Recall that the −4.0-K Jacobian matrices also have issues in reproducing the global-mean responses. We propose that using cooling SST patches is not suitable for reconstructing climate responses in AM4. A GF approach can be used properly on the premise of its success in reconstructing both global-mean and regional responses, no matter what kind of idealized experiments are performed to derive it.

d. *Sensitivity of the GF to the length of simulation and the confidence level*

In addition to the impact of the parameter A on the performance of the GF approach, it is possible that the integration

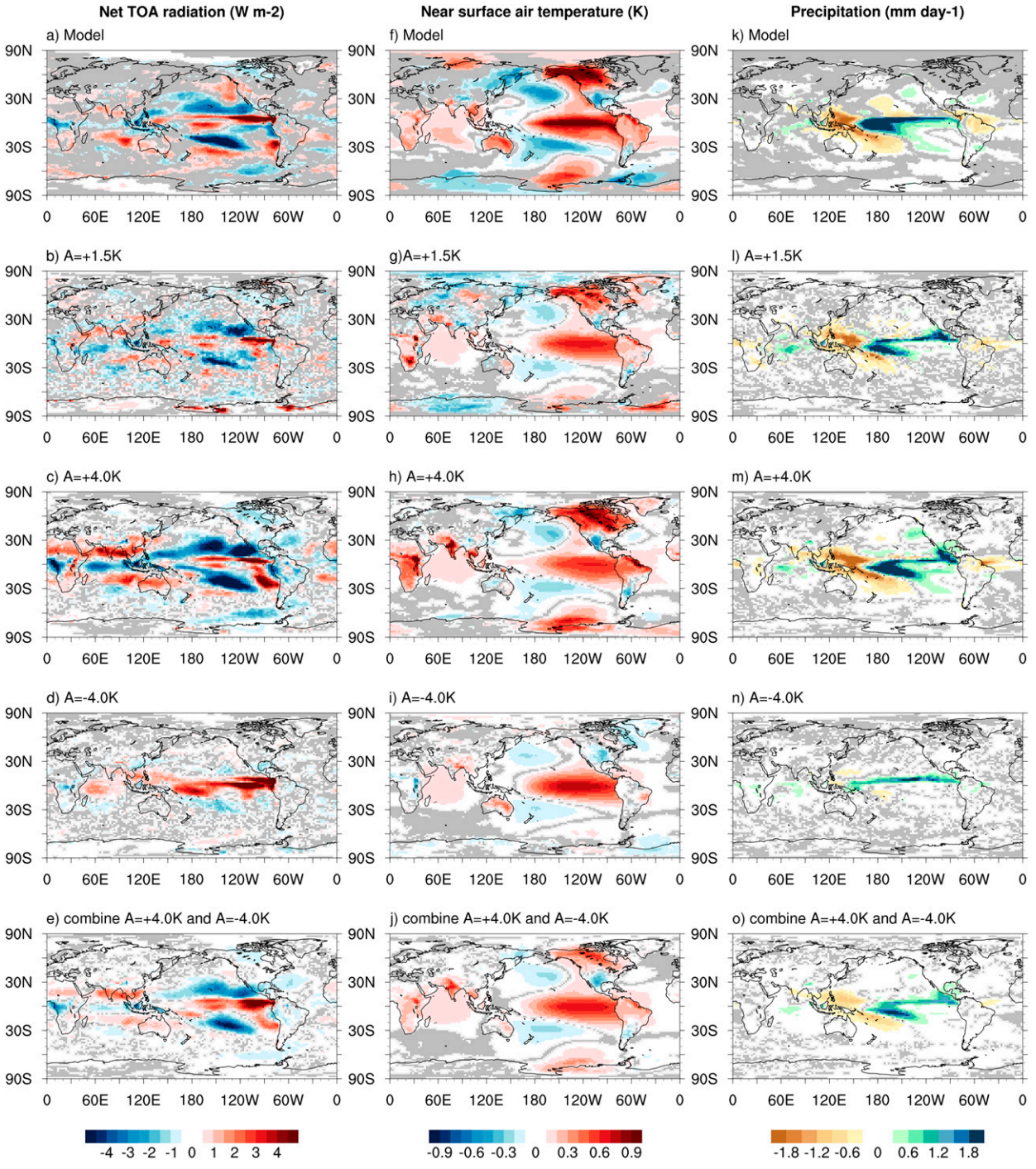

FIG. 11. Maps of (left) net TOA radiation (W m^{-2}), (center) near-surface air temperature (K), and (right) precipitation (mm day^{-1}). The results are retrieved (a),(f),(k) from the Amip-piForcing run regressed against the Niño-3.4 index and the reconstruction using the Jacobian matrices derived from experiments with (b),(g),(l) $A = +1.5$ K, (c),(h),(m) $A = +4.0$ K, and (d),(i),(n) $A = -4.0$ K, and (e),(j),(o) a combination of $A = +4.0$- and $A = -4.0$-K experiments.

time also makes a difference. As in Dong et al. (2019), the GF approach involves tests of statistical significance. Given the limited integration time, the differences between the control and SST perturbation experiments can be regarded as "noise" by the significance test with a certain confidence level. Insignificant differences are set as zero. Essentially, this is equivalent to reducing the number of grid points used for the linear sum. So far, only the Jacobian matrices derived from the 10-yr SST

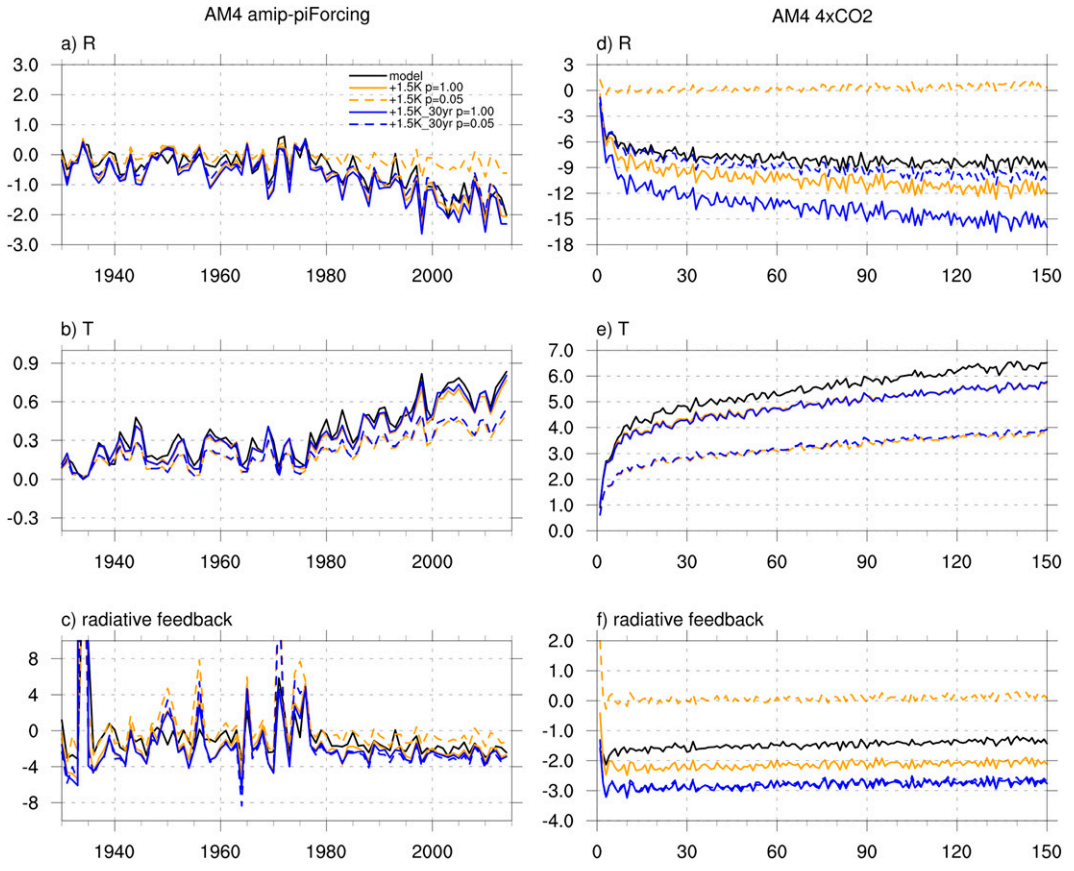

FIG. 12. As in Fig. 2, but comparing the GF reconstruction using the 10-yr Jacobian matrices with $A = +1.5$ K (orange lines), with that using the 30-yr Jacobian matrices with the same amplitude (blue lines). The solid lines are without the significance test (i.e., p value = 1.00), whereas the dash lines are with a 95% confidence level (i.e., p value = 0.05).

perturbation experiments have been considered. The relatively short integration time could be the reason why the +1.5-K Jacobian matrices with a 95% confidence level poorly reproduce the responses (Fig. 9). To examine the sensitivity of the GF to the integration time and the confidence level, we conduct another suite of SST perturbation experiments with $4 \times CO_2 = +1.5$ K and each simulation integrated for 31 years (the last 30 years are used for analyses).

As previously shown in Fig. 9, the 10-yr +1.5-K Jacobian matrices exhibit large biases with a 95% confidence level. Without the significance test, the 10-yr +1.5-K Jacobian matrices generally do a better job reproducing the model-simulated responses (Figs. 12 and 13). Nevertheless, we note that the results here only indicate that the confidence level affects the GF reconstruction when the SST perturbation experiments are integrated for a relatively short period of time. However, this does not negate the importance of the significance tests in the GF approach. We further look at the 30-yr +1.5-K Jacobian matrices. For the surface air temperature, the 10- and 30-yr Jacobian matrices show similar ability if given the same p value (Figs. 12b,e). For the net TOA radiation, the 30-yr +1.5-K Jacobian matrices with p value set as 0.05 show the best reconstruction, which is more noticeable for the AM4 $4 \times CO_2$ run (Fig. 12d). The overall better reconstruction by the 30-yr +1.5-K Jacobian matrices with p value set as 0.05 is also true for the individual components of net TOA radiation (Fig. 13). However, for the AM4 $4 \times CO_2$ run, the reconstruction of the surface air temperature still favors no significance test, even for the 30-yr Jacobian matrices (Fig. 12e). As mentioned earlier, this could be due to the fact that the impact of sea ice is not considered here.

Given a specific confidence level, the sample size is a key factor for the significance test. Since a longer simulation means a larger sample size, we argue that it would be better if the SST perturbation experiments were integrated for long periods. Generally, longer simulations help reduce potential interference from the models' internal variabilities. While it is possible that some signals would be discarded as "noise" by the significance test due to the limited sample size, longer simulations lower the risk of discarding such "signals" inadvertently. Although it is hard to find a perfect combination of the integration time and the confidence level (which requires tons of computational resources and tests), the results in this section indicate that the GF approach is sensitive to the integration time and the confidence level, which needs more attention in future studies.

However, if longer simulations of the SST perturbations experiments are not available, one may consider following

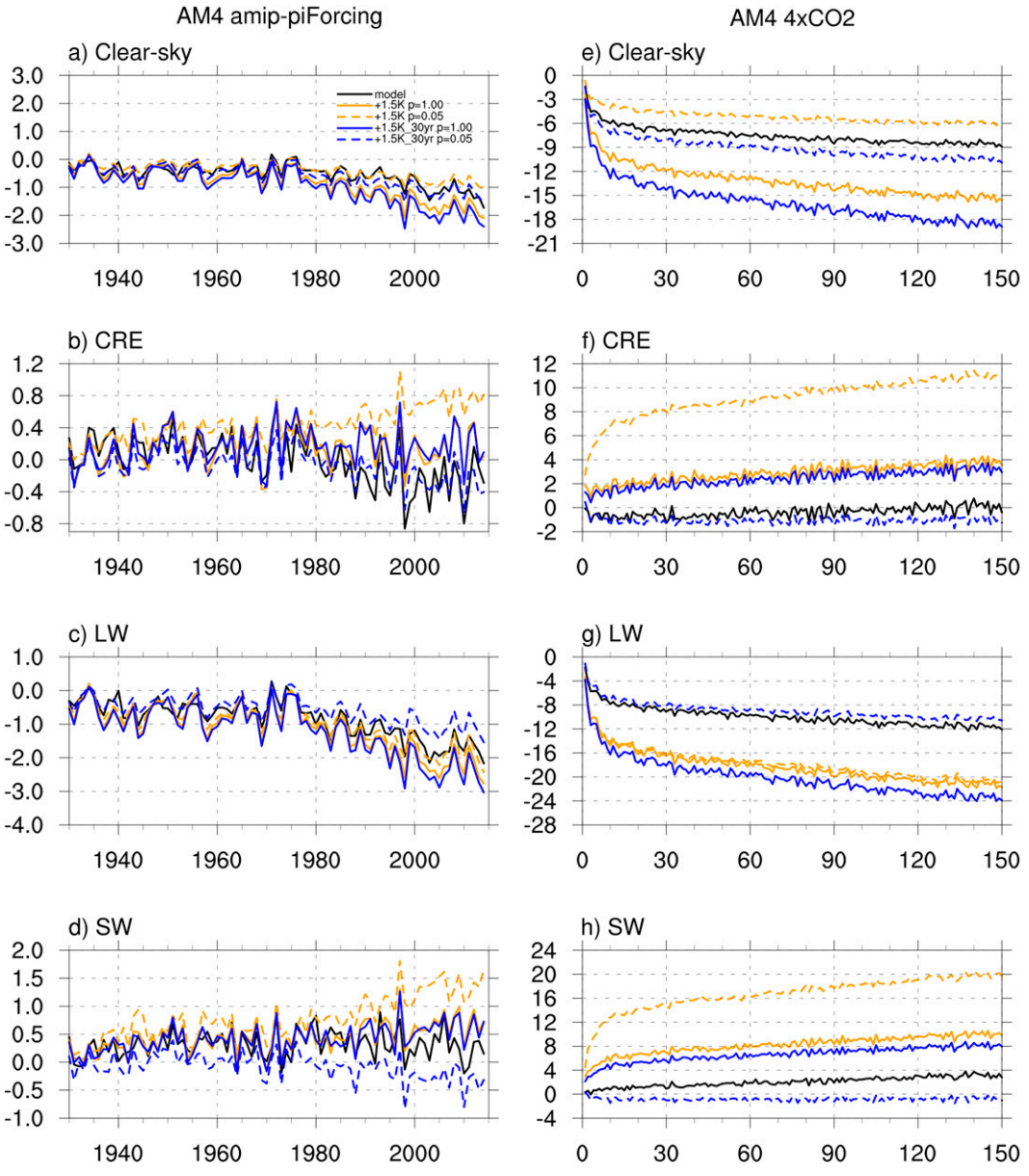

FIG. 13. As in Fig. 3, but comparing the GF reconstruction using the 10-yr Jacobian matrices with $A = +1.5$ K (orange lines), with that using the 30-yr Jacobian matrices with the same amplitude (blue lines). The solid lines are without the significance test (i.e., p value = 1.00), whereas the dash lines are with a 95% confidence level (i.e., p value = 0.05).

Eq. (5) to reproduce the responses from experiments like the AM4 4 × CO_2 run. By decomposing the total SST changes into global-mean values plus remaining anomalies, the modified GF approach significantly improves the reconstructed responses (Figs. 14 and 15).

4. Summary and discussion

In this study, we investigate the pattern effect in global climate models recently developed at NOAA's GFDL using a GF approach that utilizes several suites of idealized atmosphere-only experiments forced by patches of SST perturbations added to the present-day base state. The 10-yr +4.0-K Jacobian matrices can largely reproduce interannual variations of the global-mean radiative feedback from the AM4 Amip-piForcing run. At regional scale, the GF generally captures spatial patterns of variables associated with ENSO and IOD. In comparison, the GF reconstruction associated with AMO shows more local biases. Overall, the reconstructed responses over land exhibit more biases compared to those over ocean. It is likely that the model-simulated responses over land are affected not only by remote SST perturbations but also by local surface temperature

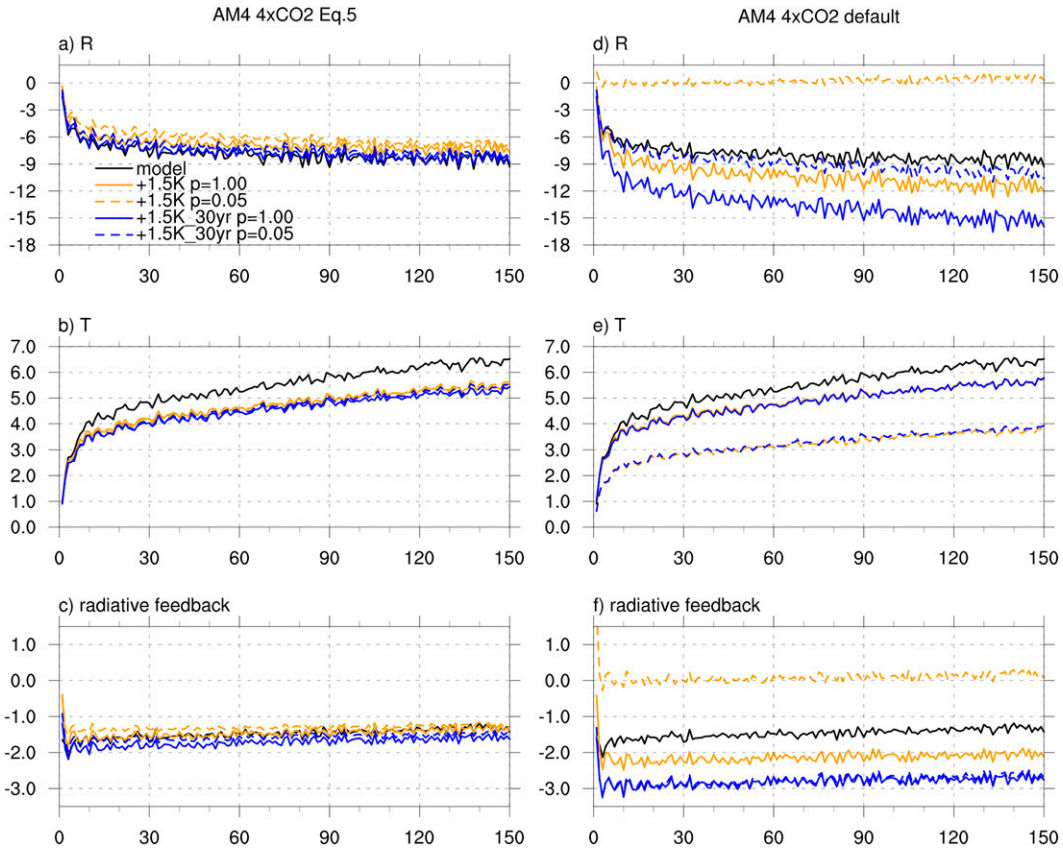

FIG. 14. The global annual-mean response for (a),(d) net TOA radiation (W m^{-2}), (b),(e) surface air temperature (K), and (c),(f) radiative feedback (W m^{-2} K^{-1}) retrieved from the AM4 4 × CO_2 run. The black solid lines show actual model simulations. The orange lines are using the 10-yr Jacobian matrices with $A = +1.5$ K, while the blue lines are using the 30-yr Jacobian matrices with the same amplitude. The solid lines are without the significance test (i.e., p value = 1.00), whereas the dash lines are with a 95% confidence level (i.e., p value = 0.05). (left) Computed using the modified GF approach following Eq. (5). (right) Computed using the default GF approach as shown in Fig. 12 but added here for reference.

changes. Since the GF approach defined by Eq. (1) treats surface temperature changes over land as "response" to SST perturbations instead of "forcing," the greater biases over land are expected to some extent. In terms of the AM4 4 × CO_2 run, the 10-yr +4.0-K Jacobian matrices have issues reproducing the magnitude of the global-mean responses. Since the AM4 4 × CO_2 run is forced by more spatially uniform SST warming, one possible way of improving the GF reconstruction is by including the contribution from the uniform warming experiments such as the Plus2K run (section 3a).

With the limited integration time, we show that the derived Jacobian matrices are sensitive to the amplitude and sign of SST perturbations. Overall, the 10-yr +4.0-K Jacobian matrices do the best in reproducing the model-simulated responses, which is more noticeable for the AM4 4 × CO_2 run. There are several potential reasons: (i) a larger absolute value of the parameter A is preferred when the integration time is not long enough but the significance test is performed. With larger SST perturbation, more grid points can pass the significance test, which reduces the loss of "information." (ii) The +4.0-K Jacobian matrices are more suitable than the −4.0-K ones for warming scenarios such as the AM4 4 × CO_2 run because the signs of temperature anomalies are more consistent between the +4.0-K SST perturbations experiments and the AM4 4 × CO_2 run.

In addition to the sign and amplitude of SST perturbations, the GF is also found to be sensitive to the integration time and significance test. A typical significance test aims at removing responses that are statistically insignificant for a given sample size. A small sample size can turn "response" into "noise." In comparison, longer simulations with a larger sample size are preferred to retain the "responses." However, the required amount of computational resources also goes up with longer simulations. This dilemma can be handled by finding a balance between the integration time and the confidence level. Nevertheless, this could vary from case to case.

We argue that the goal of the GF approach is not to perfectly reproduce the model-simulated responses but to quantify the linear part of the responses to SST perturbations. While the former requires some tuning processes to get a "good reconstruction," the latter can be regarded as an objective

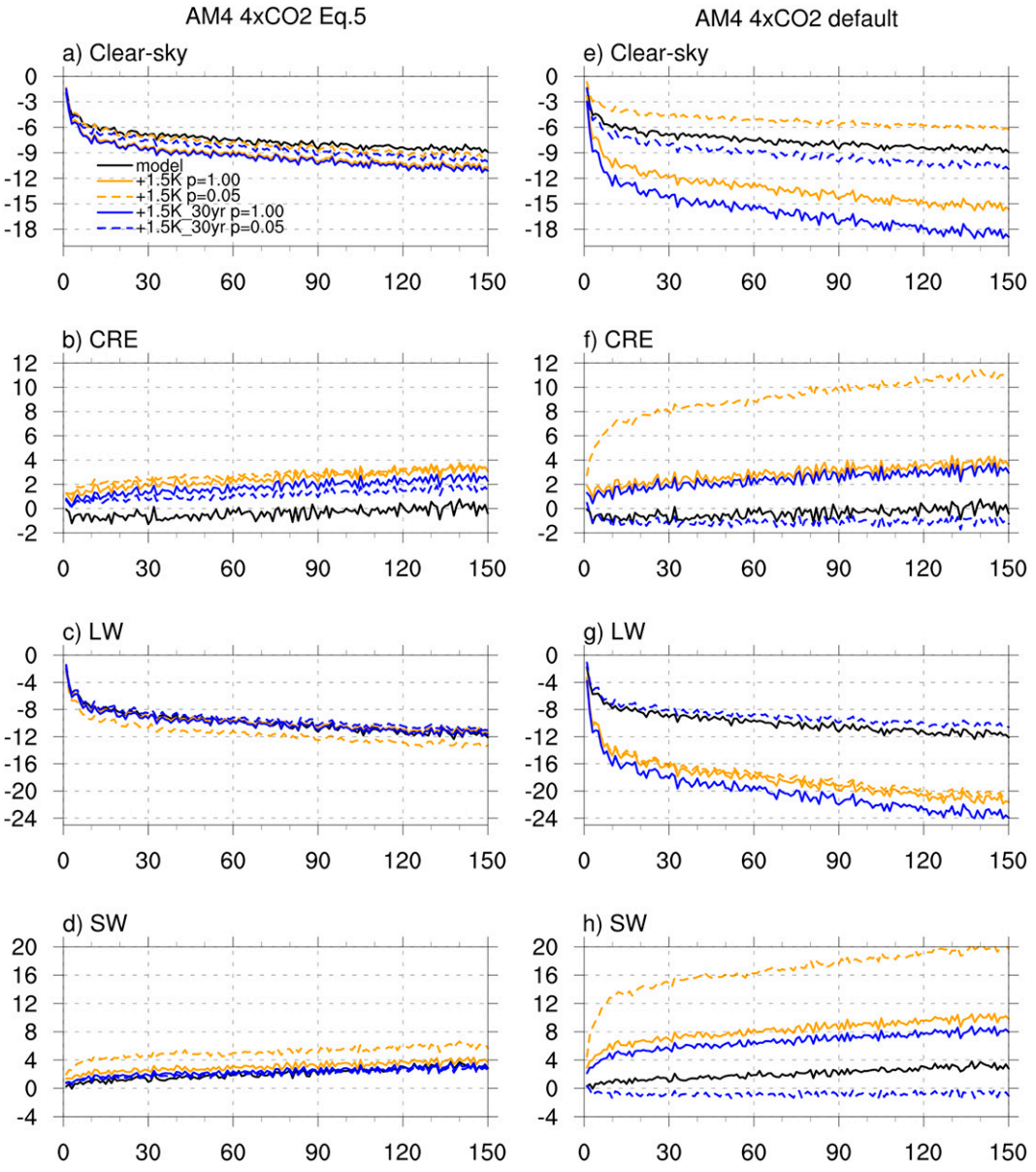

FIG. 15. As in Fig. 1, but for (a),(e) clear-sky net TOA radiation, (b),(f) cloud radiative effect, (c),(g) net LW radiation at TOA, and (d),(h) net SW radiation at TOA.

method of measuring the linear part of the SST pattern effect. Note that the nonlinear part of the responses always exists, for which the GF is not designed to solve. Moreover, it is anticipated that the Jacobian matrices would look different if the base state changed. Such state dependence is not addressed in this study but can be explored in future work.

Acknowledgments. We thank Nadir Jeevanjee, David Paynter, and Baoqiang Xiang for suggestions and comments on the initial draft of this paper. We thank two anonymous reviewers for their helpful suggestions. Discussions in the GFMIP meeting are appreciated. Support from NOAA/OAR and GFDL leadership for this project is acknowledged.

Data availability statement. The model outputs and data used in this study are available upon request.

REFERENCES

Andrews, T., and M. J. Webb, 2018: The dependence of global cloud and lapse rate feedbacks on the spatial structure of tropical Pacific warming. *J. Climate*, **31**, 641–654, https://doi.org/10.1175/JCLI-D-17-0087.1.

——, J. M. Gregory, and M. J. Webb, 2015: The dependence of radiative forcing and feedback on evolving patterns of surface temperature change in climate models. *J. Climate*, **28**, 1630–1648, https://doi.org/10.1175/JCLI-D-14-00545.1.

——, and Coauthors, 2022: On the effect of historical SST patterns on radiative feedback. *J. Geophys. Res. Atmos.*, **127**, e2022JD036675, https://doi.org/10.1029/2022JD036675.

Armour, K. C., C. M. Bitz, and G. H. Roe, 2013: Time-varying climate sensitivity from regional feedbacks. *J. Climate*, **26**, 4518–4534, https://doi.org/10.1175/JCLI-D-12-00544.1.

——, J. Marshall, J. R. Scott, A. Donohoe, and E. R. Newsom, 2016: Southern Ocean warming delayed by circumpolar upwelling and equatorward transport. *Nat. Geosci.*, **9**, 549–554, https://doi.org/10.1038/ngeo2731.

Barsugli, J. J., and P. D. Sardeshmukh, 2002: Global atmospheric sensitivity to tropical SST anomalies throughout the Indo-Pacific basin. *J. Climate*, **15**, 3427–3442, https://doi.org/10.1175/1520-0442(2002)015<3427:GASTTS>2.0.CO;2.

Bloch-Johnson, J., M. Rugenstein, and D. S. Abbot, 2020: Spatial radiative feedbacks from internal variability using multiple regression. *J. Climate*, **33**, 4121–4140, https://doi.org/10.1175/JCLI-D-19-0396.1.

Bony, S., and Coauthors, 2006: How well do we understand and evaluate climate change feedback processes? *J. Climate*, **19**, 3445–3482, https://doi.org/10.1175/JCLI3819.1.

Ceppi, P., and J. M. Gregory, 2017: Relationship of tropospheric stability to climate sensitivity and Earth's observed radiation budget. *Proc. Natl. Acad. Sci. USA*, **114**, 13 126–13 131, https://doi.org/10.1073/pnas.1714308114.

——, and S. Fueglistaler, 2021: The El Niño–Southern oscillation pattern effect. *Geophys. Res. Lett.*, **48**, e2021GL095261, https://doi.org/10.1029/2021GL095261.

Cheng, L., J. Abraham, Z. Hausfather, and K. E. Trenberth, 2019: How fast are the oceans warming? *Science*, **363**, 128–129, https://doi.org/10.1126/science.aav7619.

Dong, Y., C. Proistosescu, K. C. Armour, and D. S. Battisti, 2019: Attributing historical and future evolution of radiative feedbacks to regional warming patterns using a Green's function approach: The preeminence of the western Pacific. *J. Climate*, **32**, 5471–5491, https://doi.org/10.1175/JCLI-D-18-0843.1.

Enfield, D. B., A. M. Mestas-Nuñez, and P. J. Trimble, 2001: The Atlantic multidecadal oscillation and its relation to rainfall and river flows in the continental US. *Geophys. Res. Lett.*, **28**, 2077–2080, https://doi.org/10.1029/2000GL012745.

Eyring, V., S. Bony, G. A. Meehl, C. A. Senior, B. Stevens, R. J. Stouffer, and K. E. Taylor, 2016: Overview of the Coupled Model Intercomparison Project phase 6 (CMIP6) experimental design and organization. *Geosci. Model Dev.*, **9**, 1937–1958, https://doi.org/10.5194/gmd-9-1937-2016.

Fueglistaler, S., and L. G. Silvers, 2021: The peculiar trajectory of global warming. *J. Geophys. Res. Atmos.*, **126**, e2020JD033629, https://doi.org/10.1029/2020JD033629.

He, H., R. J. Kramer, and B. J. Soden, 2021: Evaluating observational constraints on intermodel spread in cloud, temperature, and humidity feedbacks. *Geophys. Res. Lett.*, **48**, e2020GL092309, https://doi.org/10.1029/2020GL092309.

Held, I. M., and Coauthors, 2019: Structure and performance of GFDL's CM4.0 climate model. *J. Adv. Model. Earth Syst.*, **11**, 3691–3727, https://doi.org/10.1029/2019MS001829.

Liu, M., G. Vecchi, B. Soden, W. Yang, and B. Zhang, 2021: Enhanced hydrological cycle increases ocean heat uptake and moderates transient climate change. *Nat. Climate Change*, **11**, 848–853, https://doi.org/10.1038/s41558-021-01152-0.

Luo, Y., J. Lu, F. Liu, and O. Garuba, 2017: The role of ocean dynamical thermostat in delaying the El Niño–like response over the equatorial Pacific to climate warming. *J. Climate*, **30**, 2811–2827, https://doi.org/10.1175/JCLI-D-16-0454.1.

Olonscheck, D., M. Rugenstein, and J. Marotzke, 2020: Broad consistency between observed and simulated trends in sea surface temperature patterns. *Geophys. Res. Lett.*, **47**, e2019GL086773, https://doi.org/10.1029/2019GL086773.

Rose, B. E. J., and L. Rayborn, 2016: The effects of ocean heat uptake on transient climate sensitivity. *Curr. Climate Change Rep.*, **2**, 190–201, https://doi.org/10.1007/s40641-016-0048-4.

——, K. C. Armour, D. S. Battisti, N. Feldl, and D. D. B. Koll, 2014: The dependence of transient climate sensitivity and radiative feedbacks on the spatial pattern of ocean heat uptake. *Geophys. Res. Lett.*, **41**, 1071–1078, https://doi.org/10.1002/2013GL058955.

Saji, N. H., B. N. Goswami, P. N. Vinayachandran, and T. Yamagata, 1999: A dipole mode in the tropical Indian Ocean. *Nature*, **401**, 360–363, https://doi.org/10.1038/43854.

Soden, B. J., I. M. Held, R. Colman, K. M. Shell, J. T. Kiehl, and C. A. Shields, 2008: Quantifying climate feedbacks using radiative kernels. *J. Climate*, **21**, 3504–3520, https://doi.org/10.1175/2007JCLI2110.1.

Stevens, B., S. C. Sherwood, S. Bony, and M. J. Webb, 2016: Prospects for narrowing bounds on Earth's equilibrium climate sensitivity. *Earth's Future*, **4**, 512–522, https://doi.org/10.1002/2016EF000376.

Trenberth, K. E., 1997: The definition of El Niño. *Bull. Amer. Meteor. Soc.*, **78**, 2771–2778, https://doi.org/10.1175/1520-0477(1997)078<2771:TDOENO>2.0.CO;2.

Wang, C., B. J. Soden, W. Yang, and G. A. Vecchi, 2021: Compensation between cloud feedback and aerosol-cloud interaction in CMIP6 models. *Geophys. Res. Lett.*, **48**, e2020GL091024, https://doi.org/10.1029/2020GL091024.

Watanabe, M., J.-L. Dufresne, Y. Kosaka, T. Mauritsen, and H. Tatebe, 2021: Enhanced warming constrained by past trends in equatorial Pacific sea surface temperature gradient. *Nat. Climate Change*, **11**, 33–37, https://doi.org/10.1038/s41558-020-00933-3.

Winton, M., and Coauthors, 2020: Climate Sensitivity of GFDL's CM4.0. *J. Adv. Model. Earth Syst.*, **12**, e2019MS001838, https://doi.org/10.1029/2019MS001838.

Zhang, Y., and S. Fueglistaler, 2019: Mechanism for increasing tropical rainfall unevenness with global warming. *Geophys. Res. Lett.*, **46**, 14 836–14 843, https://doi.org/10.1029/2019GL086058.

——, and ——, 2020: How tropical convection couples high moist static energy over land and ocean. *Geophys. Res. Lett.*, **47**, e2019GL086387, https://doi.org/10.1029/2019GL086387.

Zhao, M., 2022: An investigation of the effective climate sensitivity in GFDL's new climate models CM4.0 and SPEAR. *J. Climate*, **35**, 5637–5660, https://doi.org/10.1175/JCLI-D-21-0327.1.

——, and Coauthors, 2018a: The GFDL Global Atmosphere and Land Model AM4.0/LM4.0: 2. Model description, sensitivity studies, and tuning strategies. *J. Adv. Model. Earth Syst.*, **10**, 735–769, https://doi.org/10.1002/2017MS001209.

——, and Coauthors, 2018b: The GFDL Global Atmosphere and Land Model AM4.0/LM4.0: 1. Simulation characteristics with prescribed SSTs. *J. Adv. Model. Earth Syst.*, **10**, 691–734, https://doi.org/10.1002/2017MS001208.

Zhou, C., M. D. Zelinka, and S. A. Klein, 2016: Impact of decadal cloud variations on the Earth's energy budget. *Nat. Geosci.*, **9**, 871–874, https://doi.org/10.1038/ngeo2828.

——, ——, and ——, 2017: Analyzing the dependence of global cloud feedback on the spatial pattern of sea surface temperature change with a Green's function approach. *J. Adv. Model. Earth Syst.*, **9**, 2174–2189, https://doi.org/10.1002/2017MS001096.